Fragility and an extremely low shear modulus of high porosity silicic magma

Atsuko Namiki*[a], Yukie Tanaka[a], Satoshi Okumura[b], Osamu Sasaki[c], Kyohei Sano[d], Shingo Takeuchi[e]

[a]*Graduate School of Integrated Arts and Sciences, Hiroshima University, 1-7-1, Kagamiyama, Higashi Hiroshima, Hiroshima 739-8521, JAPAN*
[b]*Division of Earth and Planetary Materials Science, Department of Earth Science, Graduate School of Science, Tohoku University, Aoba 6-3, Aramaki, Aoba-ku, Sendai 980-8578, Japan*
[c]*Division of GeoEnvironmental Science, Department of Earth Science, Graduate School of Science, Tohoku University, Aoba 6-3, Aramaki, Aoba-ku, Sendai 980-8578, Japan*
[d]*Graduate School of Regional Resource Management, University of Hyogo, 128, Shounji, Toyooka, Hyogo 668-0814, Japan*
[e]*Geosphere Sciences, Civil Engineering Research Laboratory, Central Research Institute of Electric Power Industry, Abiko, Chiba 270-1194, Japan*

The rheology and strength of bubbly magma govern eruption dynamics by determining the possibility of fragmentation of ascending magmas. They are also required parameters for understanding seismic monitoring. We measured the rheology and strength of high porosity rhyolitic magma at 500-950 °C. The measured shear modulus and strength are several orders of magnitude lower than bubble-free rhyolite melt, implying that high porosity magma cannot avoid fracturing during magma ascent. The occurrence of fractures is observed in the low-temperature magma (≤800 °C). In this temperature range, the measured attenuation is low. That is, the elastic energy originated by deformations avoids attenuation and is stored in the bubbly magma until released by fracturing($Q > 1$). The newly found porosity-dependent strength based on our measurements comprehensively explains three different frag-

mentation criteria that have been previously proposed independently. Our measurements also show that the shear modulus becomes lower by increasing porosity, which can slow the shear wave velocity. These results suggest that knowing the attenuation of the seismic wave is useful to evaluate magma temperature and the possibility of a fragmentation event that may determine subsequent volcanic activities.

Keywords: magma, fracture, rheology, bubble

1. Introduction

An expansion of volcanic gas and fragmentation of surrounding magma sometimes causes hazardous explosive eruptions (e.g., Sparks, 1978; Eichelberger et al., 1986). The mechanism causing the loss of volcanic gas from the magma (outgassing) and fragmentation mechanisms have extensively been investigated (e.g., Dingwell, 1996; Papale, 1999; Zhang, 1999; Gonnermann, 2015). Two major criteria for the fragmentation of molten magma have been suggested. One is defined by a porosity threshold (volume fraction of bubbles) of $\varphi \sim 0.8$. This threshold is based on the observed upper limit of porosity in pumice (Sparks, 1978; Wilson et al., 1980). The other criterion is defined by the ratio of relaxation time τ_r relative to the deformation time scale τ_d,

$$\mathrm{De} = \frac{\tau_r}{\tau_d} = \frac{\eta_{(1/\infty)}\dot{\gamma}}{G_\infty} > 0.01. \quad (1)$$

where $\eta_{(1/\infty)}$ is magma viscosity at zero shear rate, and G_∞ is a shear modulus at an infinitely high frequency. This equation roughly indicates that if the deformation $1/\tau_d$ is sufficiently faster than the relaxation of the stress elastically stored in a Maxwell fluid with a unique relaxation time $\tau_r = \eta_{(1/\infty)}/G_\infty$,

brittle failure results (Webb and Dingwell, 1990; Cordonnier et al., 2012; Wadsworth et al., 2018). This ratio is a non-dimensional number known as the Deborah number, De. This number is sometimes called the Weissenberg number, and use of the term "Weissenberg number" is usually restricted to steady flows (e.g., Larson, 1999; Poole, 2012). Our experiments include both oscillatory and steady deformation; thus, we use the term Deborah number, hereafter. This strain rate-based criterion is frequently used to discuss outgassing from molten magmas through the fragmented surface (Castro et al., 2014; Gonnermann, 2015; Kushnir et al., 2017; Wadsworth et al., 2018).

Magmas, as a suspension of bubbles and crystals, have varying viscosity extending into several orders of magnitude, by changing temperature, composition, and the existence of crystals (e.g., James et al., 2004; Caricchi et al., 2007; Giordano et al., 2008; Mader et al., 2013). Bubbles in magma can increase and decrease the viscosity of magma with respect to the strain rate (Bagdassarov and Dingwell, 1992; Lejeune et al., 1999; Manga and Loewenberg, 2001; Llewellin et al., 2002; Stein and Spera, 2002; Vona et al., 2016). Here, the viscosity of the bubble free melt depends on its composition (including volatile content) and temperature, while the effective viscosity of the bulk magma depends also on crystals and bubbles, and strain rate. Such varying viscosity may changes relaxation time. A shear modulus, another parameter in a relaxation time, has been considered as a constant relative to a viscosity (e.g., Dingwell and Webb, 1989). The composition and water content slightly vary a shear modulus (Malfait et al., 2011; Whittington et al., 2012). In contrast, the porosity and crystalinities efficiently change a shear modulus (Bagdassarov et al., 1994; Fontaine et al., 2005; Caricchi et al.,

2008; Tripoli et al., 2016). The elasticity of a high porosity foam ($\varphi > 0.64$) is dependent on the bubble fraction and surface tension (e.g., Höhler and Cohen-Addad, 2005).

Suspensions of bubbles and crystals can have several relaxation times that differ from a simple Maxwell fluid with unique relaxation time $\tau_r = \eta_{(1/\infty)}/G_\infty$ (e.g., Namiki and Tanaka, 2017). As observed facts, the presence of crystals alters the relaxation time (Coats et al., 2018), and can modify the critical strain rate for fragmentation from Eq.(1) (Moitra et al., 2018). Thus, a high porosity magma may have different relaxation time and fragmentation criteria from a bubble-free liquid.

To quantitatively evaluate the relaxation of stress in a bubbly magma, we need to use the frequency-dependent quality factor Q, known as the inverse of attenuation. Q is a non-dimensional number and the ratio of the stored elastic energy relative to the dissipative energy (Bagdassarov and Dingwell, 1993; James et al., 2004; Namiki and Tanaka, 2017). When $Q > 1$, the stored elastic energy does not relax within the objective time scale. In contrast, when $Q < 1$, the energy imposed on the magma for the deformation dissipates viscously. Different from using the Deborah number based on the unique relaxation time τ_r, if we use frequency-dependent Q, we can evaluate multiple relaxation times through the quantitative ratio of the elastic/viscous effects as a function of the deformation time scale τ_d. The frequency-dependent rheology of magma is also required for seismological application in volcanic regions. The shear wave velocity traveling through magma depends on the shear modulus, and the attenuation of the shear wave amplitude is described by using Q (Chouet, 2003; Kumagai et al., 2014; Kawakatsu and Yamamoto,

2015).

Different from the volcanologically focused fragmentation criteria defined through the porosity and the Deborah number, rock failure is usually defined by stress or strain. The typical strength of a bubble-free magma is >100 MPa (Webb and Dingwell, 1990; Vasseur et al., 2013). The existence of bubbles can reduce the strength of magmas (Coats et al., 2018) and enhance the generation of cracks (Okumura et al., 2010; Kushnir et al., 2017). The elastic modulus decreases with an increasing number of cracks and elongated bubbles; the exact value of the decrease is affected by the orientation of the cracks and bubbles (e.g., Heap et al., 2014; Griffiths et al., 2017). Although various criteria for fragmentation/fracture have observational/experimental bases, the relationship among different criteria has not been well explained.

Outgassing by the occurrence of fragmentation has been considered (Newman et al., 1988; Rust et al., 2004; Gardner et al., 2017). However, the removal of volatiles from only a limited fractured plane through diffusion is implausible (Castro et al., 2012). To outgas the entire magma, the magma should fracture into small pieces to increase the surface area and repetitively vent from effusing lava (Castro et al., 2014).

Until now, deformation experiments on bubbly magma have been conducted for a porosity range of $\varphi < 0.7$ (Okumura et al., 2010; Pistone et al., 2012; Vona et al., 2016; Kushnir et al., 2017). It is not obvious how a highly vesiculated magma $\varphi > 0.7$ has elasticity and reduces its strength to easily fracture into small pieces to enhance outgassing. To investigate the rheology and strength of high porosity magma, we performed a series of simultaneous measurements of shear modulus, viscosity, Q, and strength. We used

an extremely high porosity ($\varphi > 0.86$) rhyolitic magma in the temperature range 500–950 °C. We explored the lower limit of the failure strength for a high porosity magma and solved the relationship among three fragmentation criteria described by porosity, the Deborah number, and stress/strain.

2. Methods

2.1. Sample preparation

In this work, we used the Tokachi-Ishizawa obsidian lava, from the Shirataki rhyolite volcanic area in northern Hokkaido, Japan. In Shirataki, dacitic and rhyolitic magma erupted during the late Pliocene, forming a caldera structure generated a pyroclastic deposit. The Tokachi-Ishizawa obsidian is aphyric rhyolitic lava at the caldera rim that erupted at ca. 2.2 Ma. Because of the elapsed time since the eruption, the upper part is eroded, and the internal structures of the lava are exposed; overall, the lava is 50 m high and 100 m wide. We collected glassy obsidian samples from the lava flow unit with neither cracks nor highly crystalline materials. The obsidian consists mainly of glass (>97%), and the effect of crystals on the rheology is negligible. The bulk silica content of this obsidian, determined using X-ray fluorescence spectrometry, is 77.8 wt.%. The silica and Al_2O_3 contents for the glass region are 77.04 wt.% and 12.40 wt.%, respectively, approximately the same as the bulk silica content. The obsidian contains microphenocrysts of magnetite (0.05–0.1 mm), microlites of plagioclase (<0.2 mm), oxides (<0.05 mm) and, rarely, K-feldspar (<0.05 mm), biotite (<0.01 mm) and plagioclase phenocrysts (0.4–1.0 mm). The water content of the obsidian samples, measured by Karl Fischer titration, is 0.5 wt.% (Sano et al., 2015).

We made foamy obsidian (perlite), which has very high porosity $\varphi > 0.86$ (Table S1), by heating the samples at 800 °C or 1000 °C for one hour. The crystal content in the foamy obsidian is low not to affect the bulk viscosity (Fig. S1). It is known that heating a hydrous rhyolite obsidian makes high porosity foam and sometimes causes explosions (Forte and Castro, 2019). The porosity increases with heating time but is difficult to control. If water remains in the sample, the sample expands during measurement. We thus used only very high porosity magma foam. Additionally, the torque range of our rheometer is low. Our rheometer is suitable for measurement of high porosity foam, which can deform at a lower stress level.

The foamy obsidian was shaped into a disc with a diameter of 25 mm and a thickness of 2.3–6.2 mm, and was used for the measurement of rheology. The approximate porosity was calculated by measuring the mass and volume of the foamy obsidian coated with a paraffin film and immersed in water. The porosities of the individual disk-shaped samples were calculated by measuring the mass and the geometrical volume of the sample and listed in Table S1.

The density of the solid part of the foamy obsidian, ρ_s = 2360 kg m^{-3}, was obtained by weighing and measuring the volume of the ground foamy obsidian using a pycnometer. The average bubble radius, assuming a spherical shape, was 660 μm. The bubble radius was calculated from the average bubble volume obtained from micro X-ray computed tomography (CT) in Fig. 1a (ScanXmate-D180RSS270, Comscantecno Co., Ltd.). The CT images (resolution of 16-20 μm/pixel) were obtained by using X-rays at accelerating voltages of 120–160 kV and a projection number of 2000.

The viscosities of the bubble-free melt with a water content of 0, 0.1

and 0.5 wt.% are estimated in Fig. S2 (Giordano et al., 2008; Romine and Whittington, 2015). Our estimated melt viscosity can vary over one order of the magnitude (Fig. S2). The melt viscosity depends both on the water content and volatile free melt composition. The water content may vary locally in the sample over 0-0.1 wt.% (Liu et al., 2005; von Aulock et al., 2017). The obsidian had microlites < 3 vol.% before the heating, and the bulk and glass compositions have a small difference. The microlites can melt during the rheology measurements at high temperature, resulting in that the glass composition may shift close to the bulk composition. We could not directly measure the viscosity of the bubble-free melt. This is because hydrous rhyolite expands during high-temperature measurements, and it is difficult to remove all bubbles from dry rhyolite after foaming.

2.2. Methods used in the shear deformation experiments

We measured the rheology of the foamy obsidian by using both steady one-directional shear deformation and oscillatory deformation (Anton paar MCR102). Steady one-directional shear deformation is intuitively understandable and frequently used for viscosity measurements. In our measurements, we placed a disc-shaped foamy obsidian sample with a thickness of h and a radius of R between two Inconel plates in a temperature-controlled oven same as used in Gonnermann et al. (2017) and Namiki et al. (2018). The surfaces of the Inconel plates have irregularities on a horizontal scale of 10–100 μm, which can be observed under the microscope. We were unable to measure the depth of the irregularities. The maximum temperature achieved by the oven is 1000 $^{\circ}$C.

From the deflection angle θ, angular velocity $\dot{\theta}$, and torque required to

deform the sample Γ, we obtain the strain γ, strain rate $\dot{\gamma}$ and shear stress σ_τ :

$$\gamma = \frac{2R\theta}{3h} \tag{2}$$

$$\dot{\gamma} = \frac{2R\dot{\theta}}{3h} \tag{3}$$

$$\sigma_\tau = \frac{4\Gamma}{3\pi R^3} \tag{4}$$

Our measurements include fractures and slips, so the obtained data sometimes appear complex. We explain the typical curves of rheological measurements in Fig. S3.

In both the one-directional deformation and oscillatory measurements, we imposed normal stresses σ_N = 10 kPa or 50 kPa. Under lower normal stress, the sample slips on the plate, so larger normal stress is preferable to prevent slipping. Concurrently, larger normal stress causes shrinkage of the sample. Besides, the maximum normal stress possibly actuating in our apparatus is 100 kPa. We chose the normal stress to satisfy these requirements. Even under these normal stresses, shrinkage of samples occurs during measurement when the sample temperature is high. To calculate the strain and strain rate, we used the time-varying height of the sample by the imposed normal stress. Porosity change during measurement was limited, as listed in Table S1.

2.2.1. One-directional deformation

By adding the shear deformation γ, and measuring the required shear stress σ_τ , we obtain the shear modulus G,

$$\sigma_\tau = G\gamma. \tag{5}$$

If the sample is an elastic material, the shear stress increases linearly with respect to strain. When fracturing occurs, the shear stress decreases. The shear stress required to deform an elastic material does not depend on the shear rate (solid curve in Fig. S3a,b).

Similarly, by adding shear deformation with a strain rate of $\dot{\gamma}$ and measuring the required shear stress, we obtain the viscosity η:

$$\sigma_\tau = \eta\dot{\gamma}. \tag{6}$$

We can also obtain the viscosity by imposing the stress and measuring the shear rate. If the sample is a purely viscous liquid (Newtonian fluid), the shear stress does not depend on strain but instead depends on the shear rate (dashed curve in Fig. S3a,b).

When the sample slides above the Inconel plate, the measured shear stress represents the friction stress

$$\sigma_\tau = \mu\sigma_{\mathrm{N}}, \tag{7}$$

where μ is the friction coefficient. As a first-order approximation, the shear stress required for frictional sliding (friction strength) does not depend on the strain and sliding velocity (dotted curve in Fig. S3a,b). In a strict sense, the friction strength depends on the sliding velocity, but we do not discuss this deeply in this study. Frictional sliding is also called slip.

When $\mu\sigma_{\mathrm{N}} > \sigma_\tau$, we can obtain the shear modulus or viscosity. In this study, we assumed $\mu \sim 0.6$ as the friction coefficient (Namiki et al., 2018).

2.2.2. Oscillatory measurements

The oscillatory rheometry imposes a sinusoidal strain $\gamma_0 e^{i\omega t}$ and measures the stress σ_τ required for deformation (e.g., Larson, 1999; Namiki and

Tanaka, 2017). This measurement provides the shear modulus, viscosity and quality factor (Q), known as the inverse of attenuation, simultaneously.

$$\sigma_\tau = |G^*|\gamma_0 e^{i(\omega t+\delta)}, \tag{8}$$

where ω is the angular frequency of oscillatory deformation, γ_0 is the strain amplitude and t is time.

$$|G^*| = G^I + iG^{II} \tag{9}$$

is the complex shear modulus. The real part is the storage modulus G^I, which is the in-phase of the strain and represents the elastic component that is similar to the shear modulus. The imaginary part is the loss modulus G^{II}, which is the in-phase of the strain rate, and indicates the viscous component that is related to the dynamic viscosity:

$$\eta^I = \frac{G^{II}}{\omega}. \tag{10}$$

The phase difference δ between the imposed strain and the measured stress is related to the ratio of the energy stored by elastic deformation to the loss of energy by dissipation, known as Q, which is the inverse of attenuation:

$$Q = \frac{1}{\tan\delta} = \frac{G^I}{G^{II}} \tag{11}$$

In a similar manner to the one-directional shear deformation measurements, we can also obtain rheological parameters by imposing the stress and measuring strain.

A more intuitive explanation for δ and Q is provided below. The elastic modulus is defined by Eq.(5). If we impose an oscillatory deformation $\gamma_0 e^{i\omega t}$ on a purely elastic material, we obtain $\sigma_\tau = G\gamma_0 e^{i\omega t}$; thus, $\delta = 0$ in Eq.(8). In

contrast, viscosity is defined by Eq.(6). If we impose an oscillatory deformation on a purely viscous material, we obtain $\sigma_\tau = i\omega\eta\gamma_0 e^{i\omega t}$; thus, $\delta = \pi/2$ in Eq.(8). We note this equation includes the relation shown in Eq.(10). Hence, we can evaluate the quantitative ratio of the elastic and viscous components by using Q obtained through δ with respect to the deformation frequency ω.

The analysis with Q is more informative than the discussion based on a unique relaxation time τ_r. By using Q, we can evaluate materials with multiple relaxation times, such as a suspension (Namiki and Tanaka, 2017), in addition to the ratio of the elastically stored energy to the dissipation. Furthermore, the measured Q consists of the seismologically obtained quality factor Q by the attenuation of the waveform. The recent seismological analysis provides local Q (Kumagai et al., 2014). To understand the material properties of seismologically observed sites, we need to obtain Q in laboratory measurements.

The shear modulus and viscosity, measured by one-directional rotation with a shear rate of $\dot{\gamma}$, are related to the complex shear modulus $G \sim |G^*|$ and the complex viscosity $\eta \sim |\eta^*| = |G^*|/\omega$ at $\omega \sim \dot{\gamma}$, respectively (Cox and Merz, 1958). When the elastic component is dominant, $G^I \gg G^{II}$, G^I approximates G, and for $G^I \ll G^{II}$, η^I approximates η. We thus use G^I and η^I in Fig. 2 and Figs. S4–S7 to evaluate the elastic and viscous components, and use $|G^*|$ and $|\eta^*|$ in Fig. 3 and 4.

Oscillatory measurements are usually plotted with respect to the angular frequency ω because of its physical background, as shown in Eqs.(8-10). However, in this paper, we plot rheological parameters as a function of a frequency of $f = \omega/(2\pi)$. This may be useful for comparison with the frequency

ranges of volcanic earthquakes.

In some of our oscillatory measurements, a reasonable pair of displacement and torque waveforms was not found. This may be attributed to the occurrence of unexpected stress/strain fluctuations. For example, if stick-slip takes place between the sample and the plates or the samples fracture, it causes sudden fluctuations of stress and strain and prevents sinusoidal deformation. In other cases, when the phase difference δ is too small, the decomposition of G^I and G^{II} is difficult. These cases were usually automatically rejected by the software of the rheometer (RheoCompass ©Anton paar). We also manually checked the waveform of the torque and rejected data where the waveforms of torque significantly deviated from the sinusoidal shape.

2.2.3. Measurement procedure

First, we placed the sample on the lower plate in the oven and then heated the oven to the desired temperature T. We waited for >15 minutes at T, which was sufficiently longer than the thermal diffusion time, then deformed the sample under specific normal stress. After the series of measurements, we cooled down the oven and observed the sample texture. The experimental conditions are summarized in Table S1.

To evaluate the sample conditions, we imposed various types of deformation: (1) frequency sweep with a constant strain amplitude of $\gamma_0 = 10^{-3}$, in which sinusoidal deformation is imposed with varying frequencies (Fig. S4); (2) strain amplitude sweep with constant frequencies of f = 1 or 10 Hz (Figs. S5 and S6); (3) frequency sweep with a constant stress amplitude of $\sigma_\tau \geq 5$ kPa (Fig. S7); and (4) one-directional shear deformation with constant shear rates or shear stresses (Fig. S8).

In deformation types (1 and 2), the rheological properties were obtained prior to fracturing, then the samples were fractured in the defromation types (3 and 4). To check the hysteresis, we applied these measurements in various combinations. When the sample thickness decreased abruptly, suggesting that the sample had fractured, we also changed the measurement combination.

The fracture occurrences are summarized in Fig. 2 and the measured raw data are shown in Figs. S4–S8.

3. Result

3.1. Deducing the deformation type from observed morphologies of measured samples

Fig. 2 summarizes the conditions used for measurements and results. Each photograph was taken after the series of rheology measurements and shows how our samples became fractured or deformed. The symbols in the top left corners of photographs indicate the deformation types and are also used in Fig. 3a. The symbols and numbers marked at the bottoms of photographs indicate the experimental conditions and the values of G^I and strength obtained by measurement. The raw data of the rheology measurements are discussed in the section "Raw data of rheology measurements" in the supplementary materials provided with Figs. S4–S8.

Fig. 2 shows that, at a lower temperature ($\leq$800 $^\circ$C), the whole sample formed small fragments in a brittle manner; i.e., the disk shape disappeared. In contrast, the hotter samples (>800 $^\circ$C) produced ash-like fragments between the sample and the plates, and sometimes shrank; that is, the disk

shape remained. In this case, the generation of fragments at high temperature is a kind of fracturing, but should be distinguished from the former case. We thus describe the colder cases as the sample exhibiting "entire fracture" and hotter cases as the sample displaying "local fracture" or "shrinkage" (Fig. 3a).

These morphologies suggest that the measured shear stresses during the rheology measurements are governed by various deformation mechanisms, which are the elastic and viscous deformations of whole samples, the friction between the unfractured sample and upper/lower plates, and the migration of the fractured samples as a granular material.

The occurrence of entire/local fracturing or shrinkage, marked at the left top of the photographs, was deduced by monitoring the normal stress and the sample thickness. For instance, in Fig. S4b and c for the colder samples, ($\leq$850 °C, bluish curves), both the normal stress and thickness are approximately constant. We thus consider that the cold samples had not yet fractured at this time. When the sample temperature is high ($\geq$900 °C, red curves), the normal stress is approximately constant, and the sample thicknesses slightly decrease, $h/h_i > 0.8$, where h_i is the initial sample thickness. We consider this result to indicate that the hot samples had shrunk without fracturing. In Fig. S7b and c, the cold samples ($\leq$800 °C, bluish curves) show a decrease in both the normal stress and their thickness $h/h_i < 0.8$; we interpret this result as meaning that the cold samples had begun to fracture entirely at this point. The fractured clasts migrated horizontally to the outside of the area below the upper plate, which in turn reduced the sample thickness (Fig. S7c). Until the upper plate moved down to maintain the

specified normal stress, the normal stress temporarily became low (Fig. S7b). This interpretation is consistent with the entirely fractured texture observed after the sequence of measurements (Fig. 2).

The difference between shrinkage and local fracturing is also evaluated by using the normal stress and the sample thickness. In Fig. S7b and c, the sample at high temperature denoted by the red circle (sample# 20180425), which had shrunk at the end (Fig. 2), exhibited a small decrease in thickness, and its normal stresses remained constant. These characteristics are consistent with the shrunken texture of the sample observed after the sequence of measurements (Fig. 1). In contrast, the sample at high temperature denoted by the red dot (sample# 20180510), which exhibited local fracturing at the end of the measurement, showed a further decrease in thickness and its normal stresses fluctuated.

3.2. Quality factor and fracture occurrence

We here compare the observed fracture types with measured Q. The fracture characteristics are well correlated with measured Q (Fig. 3b). The measurements in which the sample entirely fractured (denoted by crosses) are plotted in the region of $Q > 1$, and those in which the sample locally fractured or shrank (denoted by dots or circles) are approximately plotted in the region of $Q \leq 1$.

In Fig. 3b,c vertically arrayed symbols at the same temperature represent the frequency (strain rate) dependence. Q varies with frequency at high temperatures, but does not at low temperatures. That is, when the sample temperature is low ($<800\ ^{\circ}$C), $Q > 1$ irrespective of deformation rate, but Q for a hot sample depends on the deformation rate. For a hotter sample,

essentially, Q becomes larger with frequency (Fig. S4f). In Fig. 3b, the maximum and minimum trends of Q at each temperature indicate rapid and slow deformation, respectively. In both rapid and slow deformation trends, Q decreases with temperature.

3.3. Measured strength and shear modulus

Fig. 3c summarizes the stress level as the strength when the sample fractures or slips relative to the plate imposing the deformation. This figure also contains the measured complex modulus $|G^*|$, which is equivalent to the shear modulus G. The complex shear modulus, $|G^*|$ in Fig. 3c shows frequency dependence similar to that of Q. The maximum trend of $|G^*|$, measured at high frequencies, is within 1–100 MPa, which is more than two orders of magnitude lower than bubble-free melt (25 GPa).

The strength is illustrated in the lower half of Fig. 3c. Irrespective of the deformation type, the strengths are within 1–100 kPa, which is more than three orders of magnitude lower than the value observed for bubble-free melts ($\geq$100 MPa). The strength increases as the normal stress rises. Within the measurements under the same normal stress (10 kPa), the solid black circles in Fig. 3c show the temperature dependence. For the cold samples ($\leq 800^{\circ}$C), shear strength is lower than the normal stress imposed during the measurements. The shear strength and compressional strength are not exactly the same but may be on the same order of magnitude. We infer that the cold sample was fractured by both the vertical compression and shear stresses during the large shear deformation. We note that fracturing did not occur during the first three measurements with a small strain amplitude before conducting the measurements generated a large strain (Fig.2, sample#

20180507). Once the sample fractured as a result of the shear deformation, the sample shape became irregular and the vertical stress would have been concentrated at some restricted contact points with the bottom and top plates. This stress focusing would have enhanced the fracturing. In contrast, the strengths of the hot samples ($\geq$850 $^{\circ}$C) are higher than the normal stress. Thus, fracturing could occur only by shear deformation; as a result, the sample locally fractured and generated ash-like fragments between the sample and plates.

The ratio of the strength to the maximum $|G^*|$ is approximately 10^{-3}, suggesting that the critical strain for the fracturing of this sample is 10^{-3}.

4. Scaling for porosity dependence of rheology and fracturing

4.1. Shear modulus

The effect of bubbles on an elastic modulus is well studied in solid foams because of its relevance for engineering. The shear modulus decreases with porosity:

$$\frac{G}{G_0} = C_1(1 - \varphi)^{\alpha}, \tag{12}$$

where G_0 is the shear modulus of a bubble-free region, $1 < \alpha < 4$ and C_1 are constants (Gibson and Ashby, 1997; Roberts and Garboczi, 2001; Zheng et al., 2014). The empirical law is close to $\alpha = 2$ (Banhart and Weaire, 2002). $\alpha = 1$ is also known as the Voigt average in rock mechanics (e.g., Watt et al., 1976). For geological materials, the elastic properties of two-phase media are frequently approximated by the Hashin–Shtrikman upper bound (Hashin and Shtrikman, 1963), where, for a bubbly magma, it becomes (Manga and

Loewenberg, 2001)

$$\frac{G}{G_0} = 1 - \frac{5\varphi}{3 + 2\varphi}. \quad (13)$$

In Fig. 4a, we plot Eq.(13) and Eq.(12) for $1 < \alpha < 4$. The Hashin–Shtrikman upper bound is plotted within $1 < \alpha < 2$. Our datum (red symbol) is plotted between the curves with $2 < \alpha < 4$. This wide range of the shear modulus originates from the viscoelasticity effect and varying normal stress (Fig. 3c); in other words, our measurements include a wide range of temperature and strain rates (frequencies). Our maximum value is close to the curve for $\alpha = 2$, which is typical for a solid foam (Banhart and Weaire, 2002) and represents the result of elastic deformation, whereas the minimum represents the measurement at low frequency, in which the magma behaves more like a viscous fluid. The shear modulus measured at the higher normal stress (σ_N = 50 kPa) also shows large values (Fig. 3c). The vertical compression may thicken the thinner region (Fig. 1). The curves with $2 < \alpha < 4$ are also depicted close to the measurements with lower porosities (pink symbols) (Bagdassarov and Dingwell, 1993). The measurements of porous basalt for lower porosity denoted by the green curve (Al-Harthi et al., 1999) exhibit a slightly different trend from other curves. This may be because of the limited porosity range in their measurements ($\varphi < 0.7$). The shear modulus calculated from the Young's modulus of basaltic ash is lower than these curves (Kurokawa et al., 2017). This may be because disconnected bubble walls reduce the shear modulus.

4.2. Shear wave velocity

If the shear modulus is described by Eq.(12), the shear wave velocity becomes:

$$v_s = \sqrt{\frac{G}{\rho}} = v_{s0} \sqrt{C_1(1-\varphi)^{\alpha-1}}, \quad (14)$$

where v_{s0} is the shear velocity for a bubble-free magma. Figure 4b displays a plot of Eq.(14) and shows that the shear wave velocity can be as low as several 100 m s^{-1}.

4.3. Strength

The porosity-dependent strength of cellular material is also described by the power law of the density ratio, as shown in Eq.(12) (Zheng et al., 2014; Sypeck and Wadley, 2002; Jang et al., 2010). Typical cellular solid material has the exponent $1 < \alpha < 2$, while our measurement and other measurements with a lower porosity (Okumura et al., 2010; Coats et al., 2018) appear close to the curve with an exponent of $\alpha = 4$ (Fig. 4c). Sintered glass with porosities $\varphi > 0.2$ also exhibits similar strength (Vasseur et al., 2013). In a real magma foam, the thickness of the bubble walls and edges varies. The thinner parts should break with low stress. In contrast, cellular solids for commercial use are designed to possess strength, so walls and edges have more uniform sizes (Zheng et al., 2014). In fact, the strength of a sample under higher normal stress becomes larger, and thinner parts of the structure may become thickened (Fig. 3c).

The orange curve in Fig. 4c was obtained by rapid decompression experiments in a shock tube (Spieler et al., 2004), $1/\varphi$ MPa, and shows a different trend from other scalings. This is because the critical pressure

change to cause fragmentation by decompression is determined by the ability of the gas in the bubbles to deform the surrounding melt rather than the strength of the magma foam itself (Namiki and Manga, 2005). The green curve in Fig. 4c measured at room temperature (Al-Harthi et al., 1999) shows a slightly different trend from other curves. This may be because of the limited porosity range in those measurements ($\varphi < 0.7$), as we noted for the relative modulus. The gray curve, based the predictions by Alidibirov (1994), $200(1-\varphi^{1/3})/\varphi^{1/3}$ MPa, estimates higher values than our measurements. This may be because the gray curve assume the constant thickness of the bubble wall.

In Fig. 4c, the y-axis has a dimension because the value for normalization is not clear.

4.4. Viscosity

Various equations for the viscosity of bubbly magma are provided. The viscosity of bubbly magma depends on the shear rate. When the shear rate is slow enough, bubbles do not deform, so that the apparent viscosity becomes higher relative to the bubble-free magma (e.g., Mader et al., 2013).

When the shear rate is sufficiently high to deform bubbles, relative viscosity decreases. Pal (2003) formulates the relative viscosity at infinite shear rate as

$$\frac{\eta}{\eta_0} = \left(1 - \frac{\varphi}{\varphi_{bc}}\right)^{5\varphi_{bc}/3}, \tag{15}$$

where η_0 is the viscosity of bubble free melt. A numerical estimate of the relative viscosity for an infinite shear rate is close to the Hashin-Shtrikman upper bound (Manga and Loewenberg, 2001) which is previously introduced

in Eq.(13). Bagdassarov and Dingwell (1992) suggested an empirical equation

$$\frac{\eta}{\eta_0} = \frac{1}{1 + C\varphi}, \tag{16}$$

where $C = 22.4$ is empirically determined constant.

In Fig. 4d, our data shows larger values than these scaling. Our bubbles are deformed by compression but are not deform by shear stress (Fig. 1). We infer that the shear rate used in our experiments is lower than the infinite limit, and the effect of bubbles on viscosity is not as critical as those observed in elastic modulus and strength. We also note that the estimate of the bubble free melt viscosity includes larger uncertainties (Fig. S2).

5. Relation of three fracture criteria

We here reconsider the meaning of Eq.(1). The constitutive equation for a Maxwell fluid is written as

$$\dot{\gamma} = \frac{1}{G_\infty}\frac{d\sigma_\tau}{dt} + \frac{\sigma_\tau}{\eta_{(1/\infty)}}. \tag{17}$$

By integrating this equation with assuming a constant $\dot{\gamma}$, we obtain the strain-dependent stress

$$\sigma_\tau = \eta_{(1/\infty)}\dot{\gamma}[1 - \exp\{-\gamma/(\dot{\gamma}\tau_r)\}]. \tag{18}$$

The behavior of Eq.(18) is summarized in Fig. 5. As the strain γ increases with a constant strain rate of $\dot{\gamma}$, the stress in a Maxwell fluid accumulates and reaches an asymptotic value of $\eta_{(1/\infty)}\dot{\gamma}$. Thus, $\eta_{(1/\infty)}\dot{\gamma}$ is the maximum stress possibly accumulates in a Maxwell fluid by deformation with a constant strain rate of $\dot{\gamma}$. In this case, if there exists threshold stress for a

fracturing (strength) as denoted by the black line in Fig. 5, $\eta\dot{\gamma} >$ strength is a requirement for fracture.

The fragmentation criteria in Eq.(1), obtained for a bubble free magma, is re-written in terms of strength, $\eta_{(1/\infty)}\dot{\gamma} > 0.01 G_\infty$. Here, G_∞ is approximately constant, so that the threshold strength for fragmentation becomes a constant stress of $0.01 G_\infty$. If we use the porosity-dependent shear modulus in Eq.(12) instead of the constant G_∞, we obtain the formulation explaining our measurements shown in Fig. 4c:

$$\text{Strength} = C_2 G_0 (1-\varphi)^{a} < \eta\dot{\gamma}. \tag{19}$$

We are aware that the constant C_2 in Eq.(19) should be the critical strain that causes a fracture before stress relaxation. In our experiments, the strength was approximately three orders of magnitude lower than the shear modulus at high frequencies (Fig. 3c), suggesting that the critical strain for a fracture is 10^{-3}. The threshold of 0.01 used in Eq.(1) suggests that the critical strain for a fracture of the bubble-free melt is 10^{-2}, when viscous dissipation does not occur. Our magma foam includes small-scale structures, such as bubble walls and edges, which can locally deform and may reduce the critical strain required for fracturing. This hypothesis suggests that the constant 0.01 in Eq.(1) is not a universally applicable criterion, but a subject that can change with porosity.

Another fragmentation threshold is defined by a porosity $\varphi = 0.8$ (Sparks, 1978). By using Eq.(19), we can estimate the strength of the bubbly magma at this porosity $\varphi = 0.8$. Assuming $C_2 G_0 = 100$ MPa and $\alpha = 4$ (Fig. 4c), the estimated strength becomes 0.16 MPa. This value is three orders of magnitude lower than that of the bubble-free melt. It is reasonable to consider

that highly porous magma cannot be preserved by its fragility during magma ascent. As a result, $\varphi = 0.8$ is widely accepted as a fragmentation threshold.

A high porosity basalt (reticulite) or basaltic andesite are commonly observed in the field (e.g., Mangan and Cashman, 1996; Namiki et al., 2018). In contrast, a high porosity rhyolite is rarely found in the natural conditions (e.g., Eichelberger et al., 1986; Houghton and Wilson, 1989; Stevenson et al., 1994), but has been provided in laboratory experiments (Takeuchi et al., 2009). This may be because that bubbles in reticulites nucleated at very shallow depth so that the bubbly magma did not experience the fragmentation events. This idea is consistent with field observations. The porosity of vesicular magma found inside the silicic magma dome is <0.6 (e.g., Eichelberger et al., 1986; Stevenson et al., 1994; Noguchi et al., 2006; Sano and Toramaru, 2017), which is relatively lower than those found in fall deposits (e.g., Klug and Cashman, 1994; Houghton et al., 2010).

6. Possible conditions of magma fracture in a conduit

Our measurements show a considerable reduction in the strength of magma with increasing porosity (Fig. 4c). Although the porosity range in our measurements is quite narrow because of technical limitations, our empirical scaling is consistent with the trend for lower porosity (Fig. 4). We here apply our scaling to the fracture condition in a conduit.

In Fig. 6, we estimate the strength of bubbly magma based on the possible bubble fraction in the conduit. Fig. 6a shows the profile of porosity with depth assuming a closed system with an initial water contents of 4–7 wt.% for pre-eruptive magma, which is typical in subduction regions (e.g., Scaillet and

563 Pichavant, 2003; Takeuchi, 2011), and water solubility for rhyolite magma at
564 850 °C (Newman and Lowenstern, 2002). The estimated strength of the
565 bubbly magma is considerably reduced at a shallow depth (Fig. 6b).

566 The type of fracturing should depend on the magma temperature and
567 Q (Fig. 3). When the ascending magma is cold (T < 800 °C), Q > 1
568 even under slow deformation at 0.01 Hz (Fig. S4f). Thus the magma in the
569 shallow conduit fractures entirely (Fig. 3). Here, entire fracturing at high
570 porosity may not cause explosive eruptions. The low strength means that
571 bubbles cannot encapsulate the high-pressure gas. Even if the bubble walls
572 fracture, the gas pressure inside a bubble is low and is insufficient to cause
573 an explosion. An entire fracture in a conduit would be observed as volcanic
574 gas emissions and increases in seismicity, but the fragmented clasts may not
575 erupt out (Castro et al., 2014). If the surrounding temperature and the
576 normal stress are high enough, clasts may experience compaction to make
577 relatively drier obsidian through sintering (Newman et al., 1988; Rust et al.,
578 2004).

579 In contrast, when the ascending magma is hot, the bubbles in magma
580 deform (T > 950 °C) and the bubbly magma locally fractures near the conduit
581 wall (800 < T < 950 °C). The importance of localized shear deformation
582 around the conduit wall has been suggested (e.g., Goto, 1999; Tuffen et al.,
583 2008; Okumura et al., 2013; Gonnermann, 2015; Kushnir et al., 2017). Such
584 a banding deformation frequently observed in a complex fluids (Debrégeas
585 et al., 2001; Schall and van Hecke, 2010; Divoux et al., 2016). In a metal foam
586 as a cellular solid also shows a localized deformation in a restricted row of
587 cells (Prakash et al., 1996). Magmas may ascend in conduits intermittently

588 by stick-slip at the wall. Such a cycle of fracture and healing in magma is
589 affected by the surface morphology and healing kinetics between magma and
590 a conduit wall (e.g., Yoshimura and Nakamura, 2010; Okumura et al., 2015;
591 Lamur et al., 2019). Our experiments show that localized shear deformation
592 around the conduit wall can generate ash (Fig. 2). Ash reduces the frictional
593 strength and may cause steady sliding. In addition, the ash preserves the
594 pathway for gas flow to enhance outgassing (Okumura and Kozono, 2017).
595 The ash generated by local fracture, at high temperature and normal stress
596 conditions, plausibly undergoes sintering and makes obsidian preserving the
597 nonequilibrium degassing volatile ratio (Watkins et al., 2017).

598 Fig. 6b also shows that the strength of the bubbly magma is below the
599 friction strength (green curve) at depths shallower than 2 km. In this depth
600 range, the foamy magma inside the conduit fractures into small fragments
601 before slipping at the conduit wall. Recently, Cassidy et al. (2018) suggested
602 that an ascent velocity of 10^{-1} m s^{-1} divides the explosive/effusive transition.
603 If the shear rate, as a ratio of the ascent velocity to the conduit width, is the
604 control on fragmentation, the explosive/effusive transition should depend on
605 the conduit width. At shallow depth, the viscosity of the magma, which is
606 fully degassed under colder circumstance, would be high. The accumulated
607 stress in the ascending magma can exceed the threshold stress for fracturing.
608 Constant stress for fracturing does not necessarily depend on the conduit
609 width. The porosity dependent strength of the bubbly magma is favorable
610 to explain the independence of eruption styles with respect to shear rate.

611 Finally, we note the application for seismological observations. The low
612 shear modulus of the high porosity magma slows the shear wave velocity

(Fig. 4b). Long-period earthquakes, caused by a slow rupture or a resonance of cracks filled with bubbly magma, may be explained by this slow velocity (Chouet, 2003; Bean et al., 2013; Kawakatsu and Yamamoto, 2015). Q shows clear temperature dependence and is related to the occurrence of fractures (Fig. 3b). Thus, by monitoring Q, the temperature of a subsurface magma could be estimated. The Q beneath an active volcano is obtained by recent seismic observations (Kumagai et al., 2014). In the region beneath active fumarolic area in Taal Volcano, $Q \sim 10$ for the seismic wave frequency of $\sim$10 Hz. According to Fig. 3b, $Q \sim 10$ suggests the temperature of $\sim$700 $^{\circ}$C and the possibility of fragmentation. However, this figure includes large uncertainties. Q may depend on the magma composition. If the previously erupted pyroclastic material is heated by the intruded magma, that also shows low Q. In this case, Q can depend on the degree of sintering. These effects should be addressed. Fig. 3b also shows frequency dependence of Q. If we obtain the frequency-dependent Q structure beneath the volcanic area and the frequency and material dependence of Q measured in a laboratory, those can help to elucidate the condition beneath active volcanoes.

7. Conclusion

We measured the rheology and strength of magma with extremely high porosities (>0.86) at 500–950 $^{\circ}$C. We found that the bubbles in magma reduce the shear modulus and strength of magma by several orders of magnitude. This considerable reduction in shear modulus by the existence of bubbles slows the shear wave velocity. The extremely low strength of high porosity magma suggests that highly vesiculated magma at shallow depths is

637 certain to fracture during ascent. This hypothesis explains the fact that high
638 porosity magma ($\varphi > 0.8$) is rarely found in the field and a porosity of 0.8 has
639 been considered to be another fragmentation threshold. The quality factor Q
640 decreases with temperature increases, and the occurrence of fracturing well
641 correlates with the quality factor Q. Monitoring the shear wave velocity and
642 Q may help to estimate the porosity and temperature of magma, evaluate
643 the occurrence of fractures, and assess subsequent volcanic activities.

644 Acknowledgments

645 We thank Monodukuri Plaza at Hiroshima University for machine work of
646 our apparatus. This work is supported by JSPS KAKENHI grant 16H04042
647 and 19H00721.

648 Appendix A. Supplementary material

649 Supplementary material related to this article is provided with this manuscript.

650 References

651 Al-Harthi, A.A., Al-Amri, R.M., Shehata, W.M., 1999. The porosity and
652 engineering properties of vesicular basalt in Saudi Arabia. Engineering
653 Geology 54, 313–320. doi:10.1016/S0013-7952(99)00050-2.

654 Alidibirov, M.A., 1994. A model for viscous magma fragmenta-
655 tion during volcanic blasts. Bulletin of Volcanology 56, 459–465.
656 doi:10.1007/BF00302827.

657 von Aulock, F.W., Kennedy, B.M., Maksimenko, A., Wadsworth, F.B.,

Lavallée, Y., 2017. Outgassing from open and closed magma foams. Frontiers in Earth Science 5, 46. doi:10.3389/feart.2017.00046.

Bagdassarov, N.S., Dingwell, D.B., 1992. A rheological investigation of vesicular rhyolite. Journal of Volcanology and Geothermal Research 50, 307–322.

Bagdassarov, N.S., Dingwell, D.B., 1993. Frequency dependent rheology of vesicular rhyolite. Journal of Geophysical Research 98, 6477–6487.

Bagdassarov, N.S., Dingwell, D.B., Webb, S.L., 1994. Viscoelasticity of crystal- and bubble-bearing rhyolite melts. Physics of Earth and Planetary Interiors 83, 86–99.

Banhart, J., Weaire, D., 2002. On the road again: Metal foams find favor. Physics Today 55, 37. doi:10.1063/1.1506749.

Bean, C.J., De Barros, L., Lokmer, I., Métaxian, J.P., O' Brien, G., Murphy, S., 2013. Long-period seismicity in the shallow volcanic edifice formed from slow-rupture earthquakes. Nature Geoscience 7, 71–75. doi:10.1038/ngeo2027.

Caricchi, L., Burlini, L., Ulmer, P., 2008. Propagation of P and S-waves in magmas with different crystal contents: Insights into the crystallinity of magmatic reservoirs. Journal of Volcanology and Geothermal Research 178, 740–750. doi:10.1016/j.jvolgeores.2008.09.006.

Caricchi, L., Burlini, L., Ulmer, P., Gerya, T., Vassalli, M., Papale, P., 2007. Non-newtonian rheology of crystal-bearing magmas and implications for

magma ascent dynamics. Earth and Planetary Science Letters 264, 402–419. doi:10.1016/j.epsl.2007.09.032.

Cassidy, M., Manga, M., Cashman, Kathy Bachmann, O., 2018. Controls on explosive-effusive volcanic eruption styles. Nature Communications 9, 2839. doi:10.1038/s41467-018-05293-3.

Castro, J.M., Bindeman, I.N., Tuffen, H., Schipper, C.I., 2014. Explosive origin of silicic lava: Textural and δD-H_2O evidence for pyroclastic degassing during rhyolite effusion. Earth and Planetary Science Letters 405, 52–61. doi:10.1016/j.epsl.2014.08.012.

Castro, J.M., Cordonnier, B., Tuffen, H., Tobin, M.J., Puskar, L., Martin, M.C., Bechtel, H.A., 2012. The role of melt-fracture degassing in defusing explosive rhyolite eruptions at volcan Chaitén. Earth and Planetary Science Letters 333-334, 63–69. doi:10.1016/j.epsl.2012.04.024.

Chouet, B., 2003. Volcano seismology. pure and applied geophysics 160, 739–788. doi:10.1007/PL00012556.

Coats, R., Kendrick, J.E., Wallace, P.A., Miwa, T., Hornby, A.J., Ashworth, J.D., Matsushima, T., Lavallée, Y., 2018. Failure criteria for porous dome rocks and lavas: A study of Mt. Unzen, Japan. Solid Earth 9, 1299–1328. doi:10.5194/se-9-1299-2018.

Cordonnier, B., Caricchi, L., Pistone, M., Castro, J., Hess, K., Gottschaller, S., Manga, M., Dingwell, D., Burlini, L., 2012. The viscous-brittle transition of crystal-bearing silicic melt: Direct observation of magma rupture and healing. Geology 40, 611–614. doi:10.1130/G3914.1.

703 Cox, W.P., Merz, E.H., 1958. Correlation of dynamic and steady flow vis-
704 cosities. Journal of Polymer Science 28, 619–622.

705 Debrégeas, G., Tabuteau, H., di Meglio, J.M., 2001. Deformation and flow of
706 a two-dimensional foam under continuous shear. Physical Review Letters
707 87, 178305. doi:10.1103/PhysRevLett.87.178305.

708 Dingwell, D.B., 1996. Volcanic dilemma–flow or blow? Science 273, 1054–
709 1055.

710 Dingwell, D.B., Webb, S.L., 1989. Structural relaxation in silicate melts and
711 non-newtonian melt rheology in geologic processes. Physics and Chemistry
712 of Minerals 16, 508–516.

713 Divoux, T., Fardin, M.A., Manneville, S., Lerouge, S., 2016. Shear band-
714 ing of complex fluids. Annual Review of Fluid Mechanics 48, 81–103.
715 doi:10.1146/annurev-fluid-122414-034416.

716 Eichelberger, J.C., Carrigan, C.R., Westrich, H.R., Price, R.H., 1986. Non-
717 explosive silicic volcanism. Nature 323, 598–602. doi:10.1038/323598a0.

718 Fontaine, F.R., Ildefonse, B., Bagdassarov, N.S., 2005. Temperature depen-
719 dence of shear wave attenuation in partially molten gabbronorite at seismic
720 frequencies. Geophysical Journal International 163, 1025–1038.

721 Forte, P., Castro, J.M., 2019. H_2O - content and temperature limit the
722 explosive potential of rhyolite magma during Plinian eruptions. Earth and
723 Planetary Science Letters 506, 157–167. doi:10.1016/j.epsl.2018.10.041.

724 Gardner, J.E., Llewellin, E.W., Watkins, J.M., Befus, K.S., 2017. For-
725 mation of obsidian pyroclasts by sintering of ash particles in the vol-
726 canic conduit. Earth and Planetary Science Letters 459, 252–263.
727 doi:10.1016/j.epsl.2016.11.037.

728 Gibson, L.J., Ashby, M.F., 1997. Cellular Solids: Structure and properties,
729 2nd ed. Cambridge University Press, Cambridge, UK.

730 Giordano, D., Russell, J.K., Dingwell, D.B., 2008. Viscosity of magmatic
731 liquids: A model. Earth and Planetary Science Letters 271, 123–134.

732 Gonnermann, H.M., 2015. Magma fragmentation. Annual Review of Earth
733 and Planetary Sciences 43, 14.1–14.28.

734 Gonnermann, H.M., Giachetti, T., Fliedner, C., Nguyen, C.T., Houghton,
735 B.F., Crozier, J.A., Carey, R.J., 2017. Permeability during magma expan-
736 sion and compaction. Journal of Geophysical Research: Solid Earth 122,
737 9825–9848. doi:10.1002/2017JB014783.

738 Goto, A., 1999. A new model for volcanic earthquake at Unzen Vol-
739 cano: Melt Rupture Model. Geophysical Research Letters 26, 2541–2544.
740 doi:10.1029/1999GL900569.

741 Griffiths, L., Heap, M.J., Xu, T., feng Chen, C., Baud, P., 2017. The
742 influence of pore geometry and orientation on the strength and stiff-
743 ness of porous rock. Journal of Structural Geology 96, 149–160.
744 doi:10.1016/j.jsg.2017.02.006.

745 Hashin, Z., Shtrikman, S., 1963. A variational approach to the elastic be-
746 havior of multiphase materials. Journal of the Mechanics and Physics of
747 Solids 11, 127–140. doi:10.1016/0022-5096(63)90060-7.

748 Heap, M.J., Xu, T., Chen, C.f., 2014. The influence of porosity and vesicle
749 size on the brittle strength of volcanic rocks and magma. Bulletin of
750 Volcanology 76, 856. doi:10.1007/s00445-014-0856-0.

751 Höhler, R., Cohen-Addad, S., 2005. Rheology of liquid foam. Jour-
752 nal of Physics: Condensed Matter 17, R1041–R1069. doi:10.1088/0953-
753 8984/17/41/r01.

754 Houghton, B.F., Carey, R.J., Cashman, K.V., Wilson, C.J., Hobden, B.J.,
755 Hammer, J.E., 2010. Diverse patterns of ascent, degassing, and eruption of
756 rhyolite magma during the 1.8ka Taupo eruption, New Zealand: Evidence
757 from clast vesicularity. Journal of Volcanology and Geothermal Research
758 195, 31–47. doi:10.1016/j.jvolgeores.2010.06.002.

759 Houghton, B.F., Wilson, C.J.N., 1989. A vesicularity index for pyroclastic
760 deposits. Bulletin of Volcanology 51, 451–462. doi:10.1007/BF01078811.

761 James, M.R., Bagdassarov, N., Muller, K., Pinkerton, H., 2004. Viscoelas-
762 tic behaviour of basaltic lavas. Journal of Volcanology and Geothermal
763 Research 132, 99–113.

764 Jang, W.Y., Kyriakides, S., Kraynik, A.M., 2010. On the compressive
765 strength of open-cell metal foams with kelvin and random cell struc-
766 tures. International Journal of Solids and Structures 47, 2872–2883.
767 doi:10.1016/j.ijsolstr.2010.06.014.

768 Kawakatsu, H., Yamamoto, M., 2015. 4.15 - volcano seismology, in: Schubert,
769 G. (Ed.), Treatise on Geophysics (Second Edition). second edition ed..
770 Elsevier, Oxford, pp. 389–419. doi:10.1016/B978-0-444-53802-4.00081-6.

771 Klug, C., Cashman, K.V., 1994. Vesiculation of May 18, 1980, Mount St.
772 Helens magma. Geology 22, 468–472.

773 Kumagai, H., Lacson Jr., R., Maeda, Y., Figueroa II, M.S., Yamashina, T.,
774 2014. Shallow S wave attenuation and actively degassing magma beneath
775 Taal volcano, Philippines. Geophysical Research Letters 41, 6681–6688.

776 Kurokawa, A.K., Miwa, T., Okumura, S., Uesugi, K., 2017. Rheology of
777 basaltic ash from Stromboli volcano inferred from intermittent compression
778 experiments. Journal of Volcanology and Geothermal Research 343, 211–
779 219. doi:10.1016/j.jvolgeores.2017.07.002.

780 Kushnir, A.R., Martel, C., Champallier, R., Arbaret, L., 2017. In situ confir-
781 mation of permeability development in shearing bubble-bearing melts and
782 implications for volcanic outgassing. Earth and Planetary Science Letters
783 458, 315–326. doi:10.1016/j.epsl.2016.10.053.

784 Lamur, A., Kendrick, J.E., Wadsworth, F.B., Lavallée, Y., 2019. Fracture
785 healing and strength recovery in magmatic liquids. Geology 47, 195–198.
786 doi:10.1130/G45512.1.

787 Larson, R.G., 1999. The structure and rheology of complex fluids. Oxford
788 University Press, Oxford.

789 Lejeune, A.M., Bottinga, Y., Trull, T.W., Richet, P., 1999. Rheology of

bubble-bearing magmas. Earth and Planetary Science Letters 166, 71–84. doi:10.1016/S0012-821X(98)00278-7.

Liu, Y., Zhang, Y., Behrens, H., 2005. Solubility of H_2O in rhyolitic melts at low pressures and a new empirical model for mixed H_2OCO_2 solubility in rhyolitic melts. Journal of Volcanology and Geothermal Research 143, 219–235. doi:10.1016/j.jvolgeores.2004.09.019.

Llewellin, E.W., Mader, H.M., Wilson, S.D.R., 2002. The rheology of a bubbly liquid. Proceedings of the Royal Society of London. Series A: Mathematical, Physical and Engineering Sciences 458, 987–1016. doi:10.1098/rspa.2001.0924.

Mader, H.M., Llewellin, E.W., Mueller, S.P., 2013. The rheology of two-phase magmas: A review and analysis. Journal of Volcanology and Geothermal Research 257, 135–158. doi:10.1016/j.jvolgeores.2013.02.014.

Malfait, W.J., Sanchez-Valle, C., Ardia, P., Médard, E., Lerch, P., 2011. Amorphous materials: Properties, structure, and durability: Compositional dependent compressibility of dissolved water in silicate glasses. American Mineralogist 96, 1402–1409. doi:10.2138/am.2011.3718.

Manga, M., Loewenberg, M., 2001. Viscosity of magmas containing highly deformable bubbles. Journal of Volcanology and Geothermal Research 105, 19–24. doi:10.1016/S0377-0273(00)00239-0.

Mangan, M.T., Cashman, K.V., 1996. The structure of basaltic scoria and reticulite and inferences for vesiculation, foam formation, and fragmentation in lava fountains. J. Volcanol. Geotherm. Res. 73, 1–18.

813 Moitra, P., Gonnermann, H.M., Houghton, B.F., Tiwary, C.S., 2018. Frag-
814 mentation and plinian eruption of crystallizing basaltic magma. Earth and
815 Planetary Science Letters 500, 97–104. doi:10.1016/j.epsl.2018.08.003.

816 Namiki, A., Manga, M., 2005. Response of a bubble bearing vis-
817 coelastic fluid to rapid decompression: Implications for explosive vol-
818 canic eruptions. Earth and Planetary Science Letters 236, 269 – 284.
819 doi:10.1016/j.epsl.2005.02.045.

820 Namiki, A., Tanaka, Y., 2017. Oscillatory rheology measurements of
821 particle- and bubble-bearing fluids: Solid-like behavior of a crystal-
822 rich basaltic magma. Geophysical Research Letters 44, 8804–8813.
823 doi:10.1002/2017GL074845.

824 Namiki, A., Tanaka, Y., Yokoyama, T., 2018. Physical characteristics of
825 scoriae and ash from 2014–2015 eruption of Aso volcano, Japan. Earth,
826 Planets and Space 70, 147. doi:10.1186/s40623-018-0914-5.

827 Newman, S., Epstein, S., Stolper, E., 1988. Water, carbon dioxide, and
828 hydrogen isotopes in glasses from the ca. 1340 A.D. eruption of the mono
829 craters, california: Constraints on degassing phenomena and initial volatile
830 content. Journal of Volcanology and Geothermal Research 35, 75–96.
831 doi:10.1016/0377-0273(88)90007-8.

832 Newman, S., Lowenstern, J.B., 2002. Volatilecalc: a silicate melt -H_2O–CO_2
833 solution model written in Visual Basic for excel. Computers & Geosciences
834 28, 597–604. doi:10.1016/S0098-3004(01)00081-4.

835 Noguchi, S., Toramaru, A., Shimano, T., 2006. Crystallization of microlites
836 and degassing during magma ascent: Constraints on the fluid mechanical
837 behavior of magma during the Tenjo Eruption on Kozu Island, Japan.
838 Bulletin of Volcanology 68, 432–449. doi:10.1007/s00445-005-0019-4.

839 Okumura, S., Kozono, T., 2017. Silicic lava effusion controlled by the tran-
840 sition from viscous magma flow to friction controlled flow. Geophysical
841 Research Letters 44, 3608–3614. doi:10.1002/2017GL072875.

842 Okumura, S., Nakamura, M., Nakano, T., Uesugi, K., Tsuchiyama, A.,
843 2010. Shear deformation experiments on vesicular rhyolite: Implica-
844 tions for brittle fracturing, degassing, and compaction of magmas in
845 volcanic conduits. Journal of Geophysical Research: Solid Earth 115.
846 doi:10.1029/2009JB006904.

847 Okumura, S., Nakamura, M., Uesugi, K., Nakano, T., Fujioka, T., 2013. Cou-
848 pled effect of magma degassing and rheology on silicic volcanism. Earth and
849 Planetary Science Letters 362, 163–170. doi:10.1016/j.epsl.2012.11.056.

850 Okumura, S., Uesugi, K., Nakamura, M., Sasaki, O., 2015. Rheological tran-
851 sitions in high-temperature volcanic fault zones. Journal of Geophysical
852 Research: Solid Earth 120, 2974–2987. doi:10.1002/2014JB011532.

853 Pal, R., 2003. Rheological behavior of bubble-bearing magmas. Earth and
854 Planetary Science Letters 207, 165–179.

855 Papale, P., 1999. Strain-induced magma fragmentation in explosive erup-
856 tions. Nature 397, 425–428. doi:10.1038/17109.

857 Pistone, M., Caricchi, L., Ulmer, P., Burlini, L., Ardia, P., Reusser, E.,
858 Marone, F., Arbaret, L., 2012. Deformation experiments of bubble- and
859 crystal-bearing magmas: Rheological and microstructural analysis. Jour-
860 nal of Geophysical Research: Solid Earth 117. doi:10.1029/2011JB008986.

861 Poole, R.J., 2012. The deborah and weissenberg numbers. The British Society
862 of Rheology, Rheology Bulletin 53, 32–39.

863 Prakash, O., Bichebois, P., Brechet, Y., Louchet, F., Embury, J.D.,
864 1996. A note on the deformation behaviour of two-dimensional
865 model cellular structures. Philosophical Magazine A 73, 739–751.
866 doi:10.1080/01418619608242994.

867 Roberts, A.P., Garboczi, E.J., 2001. Elastic moduli of model random
868 three-dimensional closed-cell cellular solids. Acta Materialia 49, 189–197.
869 doi:10.1016/S1359-6454(00)00314-1.

870 Romine, W.L., Whittington, A.G., 2015. A simple model for the vis-
871 cosity of rhyolites as a function of temperature, pressure and wa-
872 ter content. Geochimica et Cosmochimica Acta 170, 281 – 300.
873 doi:10.1016/j.gca.2015.08.009.

874 Rust, A.C., Cashman, K.V., Wallace, P.J., 2004. Magma degassing buffered
875 by vapor flow through brecciated conduit margins. Geology 32, 349–352.
876 doi:10.1130/G20388.2.

877 Sano, K., Toramaru, A., 2017. Cooling and crystallization of rhyolite-
878 obsidian lava: Insights from micron-scale projections on plagioclase mi-

crolites. Journal of Volcanology and Geothermal Research 341, 158–171. doi:10.1016/j.jvolgeores.2017.05.012.

Sano, K., Wada, K., Sato, E., 2015. Rates of water exsolution and magma ascent inferred from microstructures and chemical analyses of the Tokachi-Ishizawa obsidian lava, Shirataki, northern Hokkaido, Japan. Journal of Volcanology and Geothermal Research 292, 29–40.

Scaillet, B., Pichavant, M., 2003. Experimental constraints on volatile abundances in arc magmas and their implications for degassing processes. Geological Society, London, Special Publications 213, 23–52. doi:10.1144/GSL.SP.2003.213.01.03.

Schall, P., van Hecke, M., 2010. Shear bands in matter with granularity. Annual Review of Fluid Mechanics 42, 67–88. doi:10.1146/annurev-fluid-121108-145544.

Sparks, R.S.J., 1978. The dynamics of bubble formation and growth in magmas: A review and analysis. Journal of Volcanology and Geothermal Research 3, 1–37. doi:10.1016/0377-0273(78)90002-1.

Spieler, O., Kennedy, B., Kueppers, U., Dingwell, D.B., Scheu, B., Taddeucci, J., 2004. The fragmentation threshold of pyroclastic rocks. Earth and Planetary Science Letters 226, 139–148. doi:10.1016/j.epsl.2004.07.016.

Stein, D.J., Spera, F.J., 2002. Shear viscosity of rhyolite-vapor emulsions at magmatic temperatures by concentric cylinder rheometry. Journal of Volcanology and Geothermal Research 113, 243–258. doi:10.1016/S0377-0273(01)00260-8.

902 Stevenson, R.J., Briggs, R.M., Hodder, A.P.W., 1994. Physical volcanology
903 and emplacement history of the Ben Lomond rhyolite lava flow, Taupo
904 Volcanic Centre, New Zealand. New Zealand Journal of Geology and Geo-
905 physics 37, 345–358. doi:10.1080/00288306.1994.9514625.

906 Sypeck, D.J., Wadley, H.N.G., 2002. Cellular metal truss core sandwich
907 structures. Advanced Engineering Materials 4, 759–764.

908 Takeuchi, S., 2011. Preeruptive magma viscosity: An important measure of
909 magma eruptibility. Journal of Geophysical Research: Solid Earth 116.
910 doi:10.1029/2011JB008243.

911 Takeuchi, S., Tomiya, A., Shinohara, H., 2009. Degassing conditions for
912 permeable silicic magmas: Implications from decompression experiments
913 with constant rates. Earth and Planetary Science Letters 283, 101–110.
914 doi:10.1016/j.epsl.2009.04.001.

915 Tripoli, B.A., Cordonnier, B., Zappone, A., Ulmer, P., 2016. Ef-
916 fects of crystallization and bubble nucleation on the seismic proper-
917 ties of magmas. Geochemistry, Geophysics, Geosystems 17, 602–615.
918 doi:10.1002/2015GC006123.

919 Tuffen, H., Smith, R., Sammonds, P.R., 2008. Evidence for seismogenic
920 fracture of silicic magma. Nature 453, 511–515. doi:10.1038/nature06989.

921 Vasseur, J., Wadsworth, F.B., Lavallée, Y., Hess, K.U., Dingwell,
922 D.B., 2013. Volcanic sintering: Timescales of viscous densification
923 and strength recovery. Geophysical Research Letters 40, 5658–5664.
924 doi:10.1002/2013GL058105.

925 Vona, A., Ryan, A.G., Russell, J.K., Romano, C., 2016. Models for viscosity
926 and shear localization in bubble-rich magmas. Earth and Planetary Science
927 Letters 449, 26–38. doi:10.1016/j.epsl.2016.05.029.

928 Wadsworth, F.B., Witcher, T., Vossen, C.E.J., Hess, K., Unwin, H.E., Scheu,
929 B., Castro, J.M., Dingwell, D.B., 2018. Combined effusive-explosive silicic
930 volcanism straddles the multiphase viscous-to-brittle transition. Nature
931 Communications 9, 4696. doi:10.1038/s41467-018-07187-w.

932 Watkins, J.M., Gardner, J.E., Befus, K.S., 2017. Nonequilibrium degassing,
933 regassing, and vapor fluxing in magmatic feeder systems. Geology 45,
934 183–186. doi:10.1130/G38501.1.

935 Watt, J.P., Davies, G.F., O'Connell, R.J., 1976. The elastic prop-
936 erties of composite materials. Reviews of Geophysics 14, 541–563.
937 doi:10.1029/RG014i004p00541.

938 Webb, S.L., Dingwell, D.B., 1990. Non-newtonian rheology of igneous melts
939 at high stresses and strain rates: Experimental results for rhyolite, an-
940 desite, basalt, and nephelinite. Journal of Geophysical Research: Solid
941 Earth 95, 15695–15701. doi:10.1029/JB095iB10p15695.

942 Whittington, A.G., Richet, P., Polian, A., 2012. Water and the compress-
943 ibility of silicate glasses: A brillouin spectroscopic study. American Min-
944 eralogist 97, 455–467. doi:10.2138/am.2012.3891.

945 Wilson, L., Sparks, R.S.J., Walker, G.P.L., 1980. Explosive volcanic erup-
946 tions - IV. The control of magma properties and conduit geometry on

947 eruption column behaviour. Geophysical Journal of the Royal Astronomi-
948 cal Society 63, 117–148. doi:10.1111/j.1365-246X.1980.tb02613.x.

949 Yoshimura, S., Nakamura, M., 2010. Fracture healing in a magma:
950 An experimental approach and implications for volcanic seismicity
951 and degassing. Journal of Geophysical Research: Solid Earth 115.
952 doi:10.1029/2009JB000834.

953 Zhang, Y., 1999. A criterion for the fragmentation of bubbly magma based
954 on brittle failure theory. Nature 402, 648–650. doi:10.1038/45210.

955 Zheng, X., Lee, H., Weisgraber, T.H., Shusteff, M., DeOtte, J., Duoss, E.B.,
956 Kuntz, J.D., Biener, M.M., Ge, Q., Jackson, J.A., Kucheyev, S.O., Fang,
957 N.X., Spadaccini, C.M., 2014. Ultralight, ultrastiff mechanical metamate-
958 rials. Science 344, 1373–1377. doi:10.1126/science.1252291.

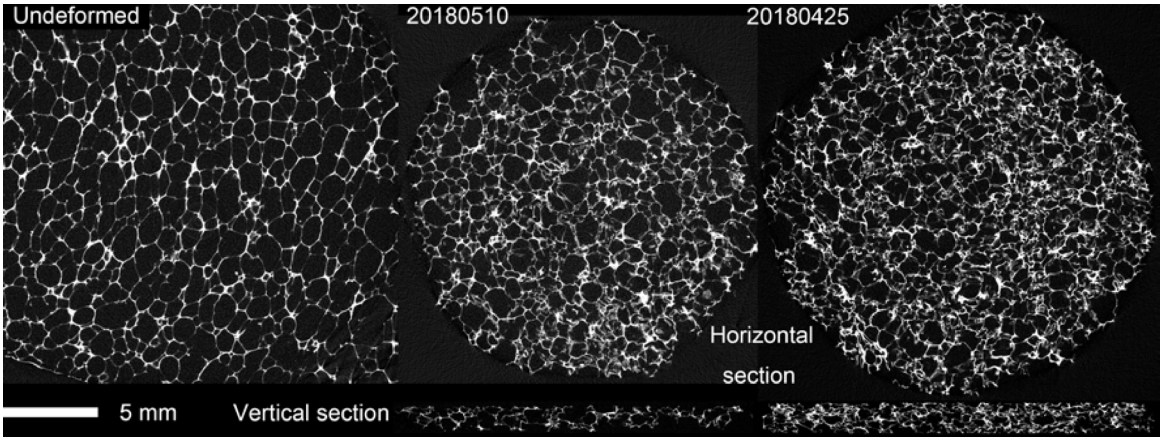

Figure 1: X-ray computed tomography (CT) images of the samples in horizontal cross-sectional views, (left) sample baked at 1000 °C before the rheology measurements, (middle) sample subjected to a temperature of 950 °C and σ_N = 10 kPa, and (right) sample subjected to a temperature of 950 °C and σ_N = 50 kPa. Bottom pictures are vertical cross-sectional views. The whitish parts indicate melt/solid; black parts represent pores.

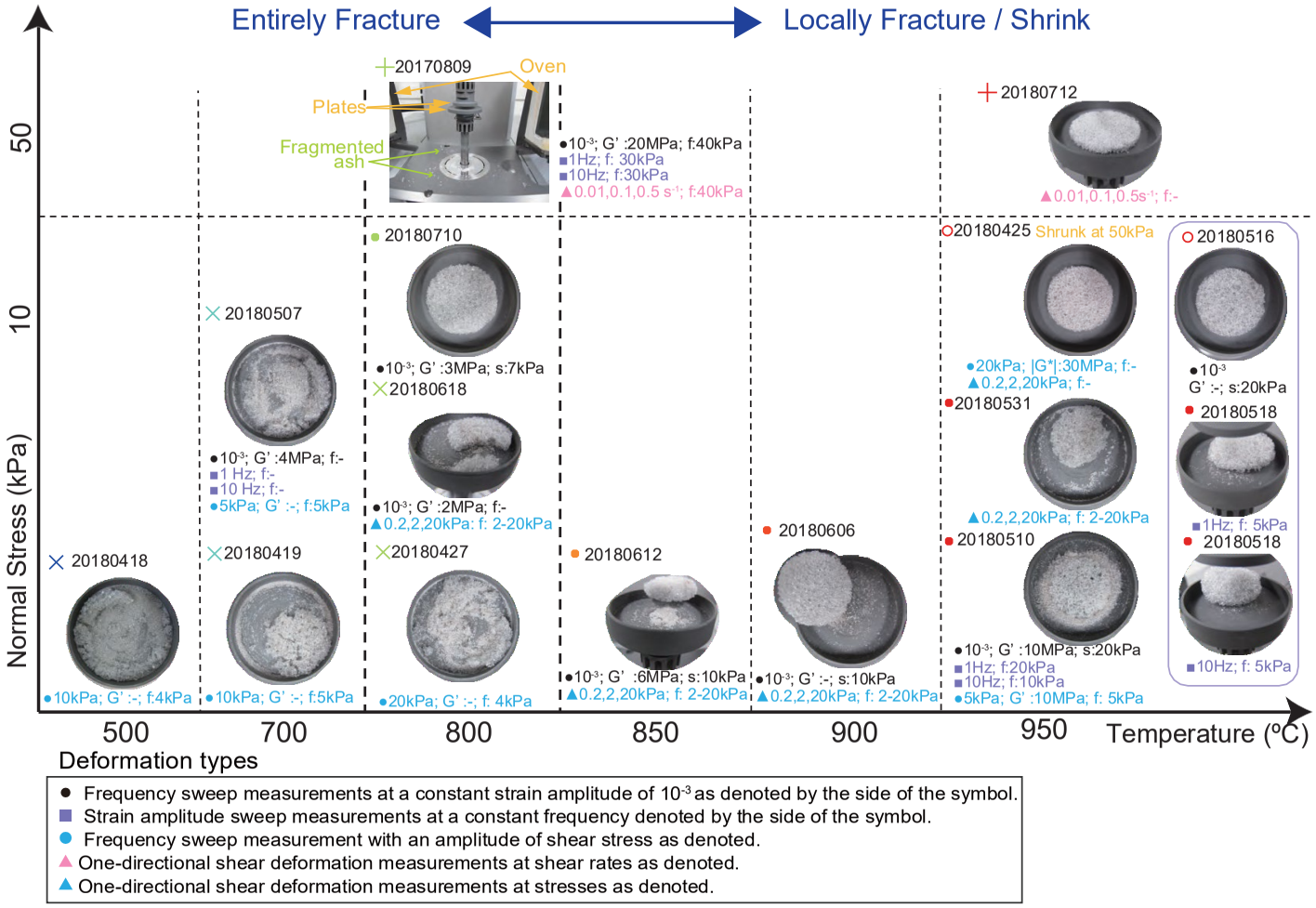
Entirely Fracture
Locally Fracture / Shrink
Normal Stress (kPa)
50
10
Temperature (°C)
500
700
800
850
900
950
20170809
Oven
Plates
Fragmented ash
●10-3; G' :20MPa; f:40kPa
■1Hz; f: 30kPa
■10Hz; f:30kPa
▲0.01,0.1,0.5 s-1; f:40kPa
20180712
▲0.01,0.1,0.5s-1; f:-
20180425 Shrunk at 50kPa
●20kPa; |G*|:30MPa; f:-
▲0.2,2,20kPa; f:-
20180516
●10-3
G' :-; s:20kPa
20180518
■1Hz; f: 5kPa
20180518
■10Hz; f: 5kPa
20180710
●10-3; G' :3MPa; s:7kPa
20180618
●10-3; G' :2MPa; f:-
▲0.2,2,20kPa: f: 2-20kPa
20180507
●10-3; G' :4MPa; f:-
■1 Hz; f:-
■10 Hz; f:-
●5kPa; G' :-; f:5kPa
20180531
▲0.2,2,20kPa; f: 2-20kPa
20180510
●10-3; G' :10MPa; s:20kPa
■1Hz; f:20kPa
■10Hz; f:10kPa
●5kPa; G' :10MPa; f: 5kPa
20180606
●10-3; G' :-; s:10kPa
▲0.2,2,20kPa; f: 2-20kPa
20180612
●10-3; G' :6MPa; s:10kPa
▲0.2,2,20kPa; f: 2-20kPa
20180418
●10kPa; G' :-; f:4kPa
20180419
●10kPa; G' :-; f:5kPa
20180427
●20kPa; G' :-; f: 4kPa
Deformation types
● Frequency sweep measurements at a constant strain amplitude of 10-3 as denoted by the side of the symbol.
■ Strain amplitude sweep measurements at a constant frequency denoted by the side of the symbol.
● Frequency sweep measurement with an amplitude of shear stress as denoted.
▲ One-directional shear deformation measurements at shear rates as denoted.
▲ One-directional shear deformation measurements at stresses as denoted.

Figure 2: Summary of our rheology measurements. Each photograph shows the sample after the series of rheology measurements under various temperatures and normal stresses. The whitish part is foamy obsidian with an initial diameter of 25 mm, which is on an Inconel plate with an inner diameter of 36 mm. Colder samples were entirely fractured into small clasts, whereas the hotter samples shrank or generated ash-like fragments by local fracturing. In some photographs, the disc-shaped sample was artificially moved to show the fragments generated by shear deformation. The symbols marked at the bottoms of photographs indicate the conditions used in the rheology measurement, as shown in the legend. The value of G' measured as the shear modulus at 1 Hz is denoted by "G' ". The shear stress as the friction (slip) strength, at which the stress suddenly decreases in Fig. S4a, is denoted by "s". The shear stress as the entire/local fracture (fracture strength), at which the stress suddenly decreases in Fig. S7a or Fig. S8a, is denoted by "f". A hyphen "-" indicates there are no reliable data. The number at the top left of each photograph is the sample number. The symbols on the left side of each sample number are used in Figs. 3 and S4–S8, and indicate the type of deformation. Crosses and the green plus signs indicate that the sample entirely fractured during measurement under the normal stresses of 10 kPa and 50 kPa, respectively. Dots indicate that ash-like fragments were generated by local fracturing, sometimes with shrinkage. Circles indicate that the sample shrank without entire/local fracturing. The symbol color indicates temperature. The red plus indicates shrinkage under a normal stress of 50 kPa. In measurement 20170809, the sample, which was sandwiched between two flat plates, fragmented into small clasts and was blown out by circulating air in the oven, and was observed as scattered ash on the floor. After that, we used a plate with an edge as the lower plate to preserve the clasts produced.

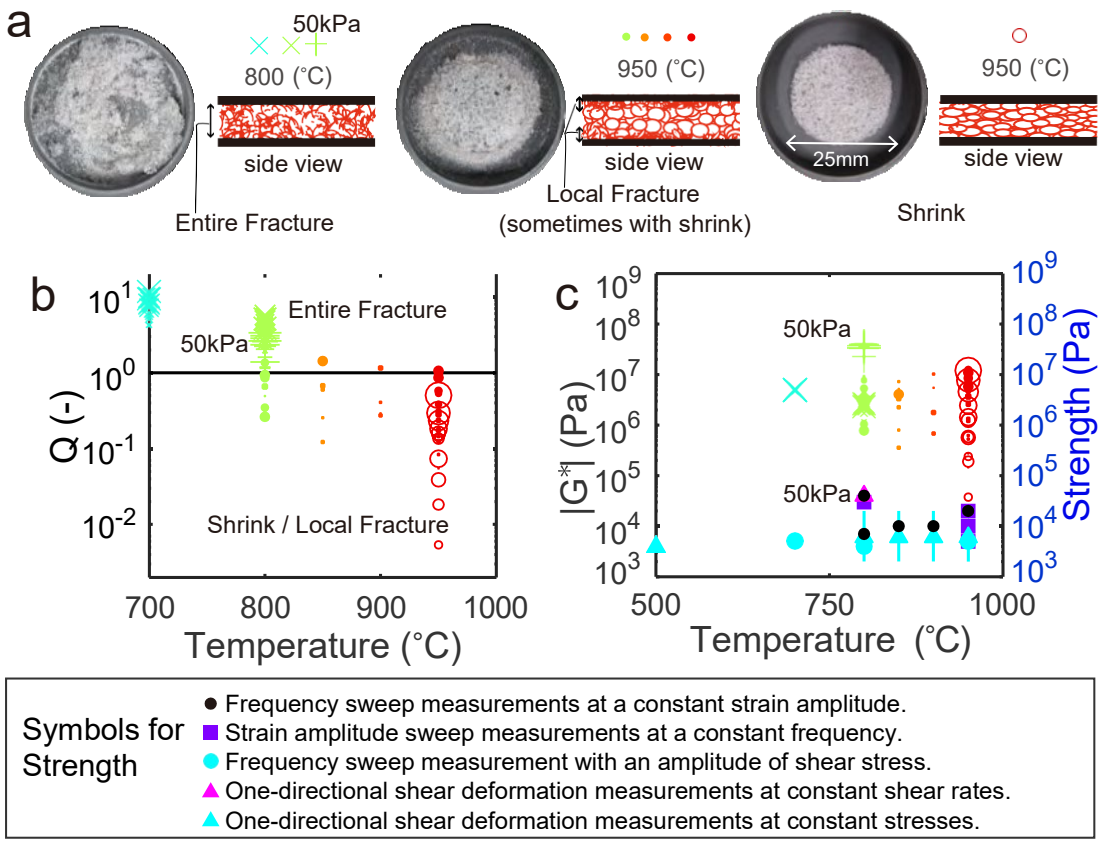

960

961 Figure 3

Figure 3: Relation between rheology and fracture types at various temperatures. (a) Fracture types varying with temperature after the series of rheology measurements. In the photographs, the whitish part is the foamy obsidian sample with an initial diameter of 25 mm on the bottom plate. The schematic illustration shows fractured regions and deformation of the samples in side view during deformation. The symbols above the illustration denote the fracture types and are used in parts (b), (c) and Fig. 2, in which larger symbols represent measurements at higher frequencies. The symbol color indicates the temperature. The notation "50kPa" above the plus sign indicates measurement at higher normal stress (σ_N = 50 kPa). The others denote measurement at σ_N = 10 kPa. (b) Q for the frequency range <1 Hz obtained by the frequency sweep measurements at a constant strain amplitude (Fig. S4). Q depends on the deformation frequency, so symbols for different frequencies are arrayed vertically at the same temperature. Essentially, Q becomes larger with frequency and exhibits greater variation at higher temperatures. (c) Strength and complex modulus $|G^*|$, which is equivalent to the shear modulus. $|G^*|$ is plotted with the same symbols defined in (a). The strengths appear in the low-stress region ($<10^5$ Pa) and are measured by various deformation types, as classified by the symbols explained below this panel. The values of strength are denoted in Fig. 2. Original data are shown in Figs. S4–S8.

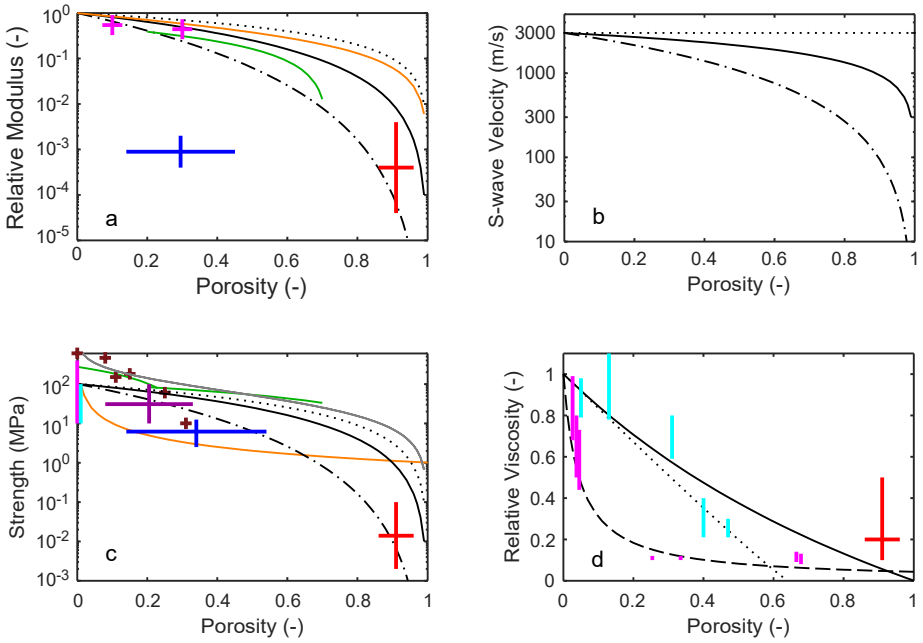

962

963 Figure 4

Figure 4: Scalings relative to the porosity. (a) Relative shear modulus to G_0 = 25 GPa versus porosity. The red symbol indicates our measurement (G = 1–100 MPa). The pink symbols are from other obsidians (Bagdassarov and Dingwell, 1993). The dotted, solid and dash-dotted black curves show α = 1, 2 and 4 in Eq.(12), respectively, and C_1 = 1. The orange curve plots Eq.(13) and the green curve shows other empirical scalings (Al-Harthi et al., 1999). (b) Calculated shear wave velocity using Eq.(14) with an assumption of v_{s0} = 3 km s^{-1}. The line styles are the same as in (a). (c) Strength versus porosity. The red symbol indicates our measurement (2–100 kPa). The blue symbol is another obsidian calculated from the viscosity at 830 $^\circ$C (Okumura et al., 2010). The purple symbol shows the failure condition for dacite lava from Mt. Unzen (Coats et al., 2018). The brown pluses show the uniaxial compressive strength of sintered glass (Vasseur et al., 2013) The light blue (Cordonnier et al., 2012) and pink symbols (Webb and Dingwell, 1990) show bubble-free magma. The dotted, solid, and dash-dotted black curves show α = 1.5, 2, 4 in Eq.(12), respectively, and C_1 = 1. The green (Al-Harthi et al., 1999), orange (Spieler et al., 2004), and gray curves (Alidibirov, 1994) are other equations. (d) Relative viscosity versus porosity. The red symbol indicates our measurement ($\eta = 10^7 - 5 \times 10^7$ Pa s) for 950 $^\circ$C. We use 10^8 Pa s to normalize our data, which consists of the dry bulk composition or glass composition with 0.1 wt.% water in Fig. S2. The pink (Bagdassarov and Dingwell, 1993) and light blue symbols (Lejeune et al., 1999) show values from previous studies. The solid, dotted, and dashed curves plot Eqs.(13, 15, and 16), respectively.

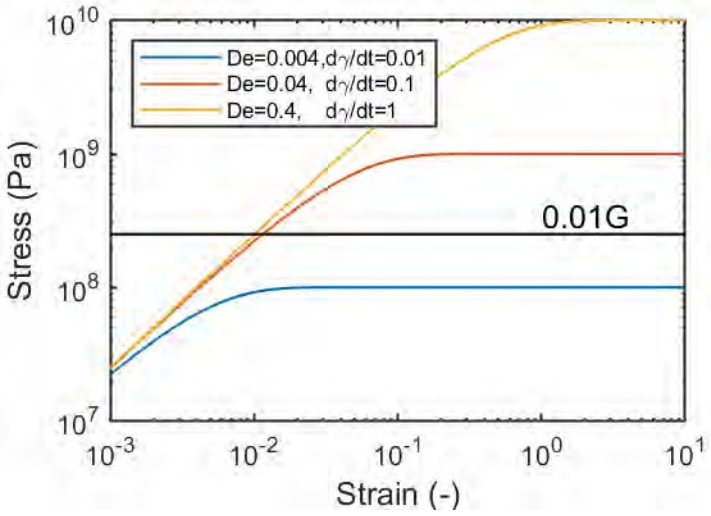

Figure 5: The evolution of stored stress in a Maxwell fluid respect to increasing strain with certain strain rates, calculated by Eq.(18). We here assume G_∞ = 25 GPa, and $\eta_{(1/\infty)}$ = 10^{10} Pa s.

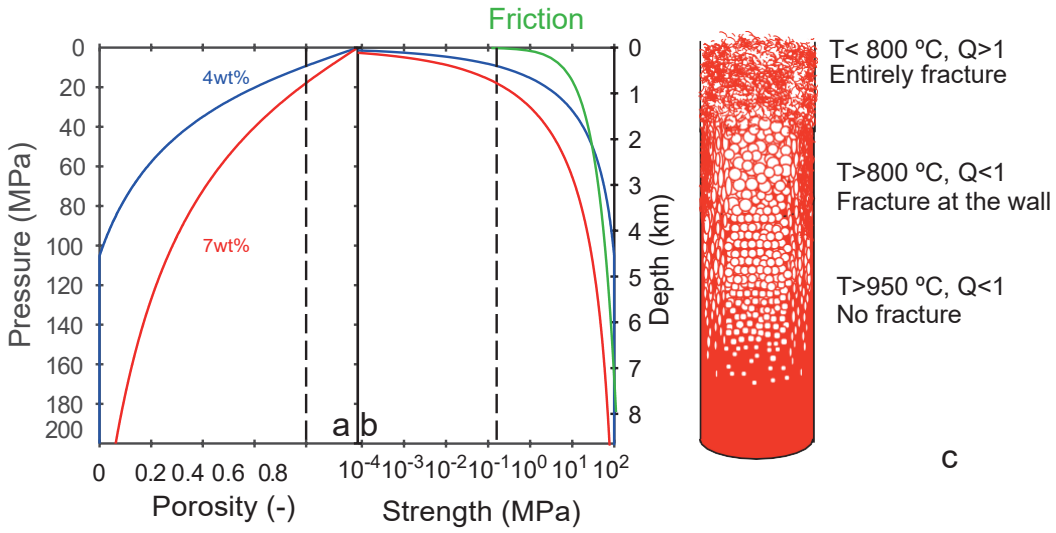

Figure 6: Occurrence fracturing of ascending magma within a conduit. (a) Porosity φ with varying pressure without outgassing (closed system). The blue and red curves indicate the initial water content of 4 and 7 wt.%, respectively. The water density is calculated by assuming an ideal gas. The black dashed line is the reference for $\varphi = 0.8$. (b) Estimated strength of bubbly magma by using Eq.(19) with $\alpha = 4$ and $C_2G_0 = 100$ MPa. Blue, red and black curves are the same as in (a). The green curve is the friction strength calculated with a friction coefficient of 0.6. The right-side y-axis is scaled by assuming lithostatic pressure with a rock density of 2360 kg m^{-3}. (c) Illustration of a possible state in a shallow conduit.

Table S1: Conditions of measurements.

Run #	Measured T	Baked T	σ_N	2R	h_i	h_f**	ρ	Initial ϕ	Shrunk ϕ***
	°C	°C	kPa	mm	mm	mm	kg/m^3		
20180418	500	1000	10	24.2	5.28	-	102	0.96	-
20180419	700	1000	10	24.2	5.51	-	92	0.96	-
20180507	700	1000	10	24.2	4.69	-	83	0.96	-
20180427	800	1000	10	23.4	6.14	-	83	0.96	-
20180618	800	1000	10	24.2	4.89	4.82	109	0.95	0.95
20180710	800	1000	10	24.5	5.35	5.26	102	0.96	0.96
20170809	800	800	50	24.6	3.96	-	132	0.94	-
20180612	850	1000	10	24.4	4.88	4.75	108	0.95	0.95
20180606	900	1000	10	23.8	5.79	5.41	108	0.95	0.95
20180531	950	1000	10	24.0	5.01	3.72	189	0.92	0.89
20180518	950	1000	10	24.1	4.53	4.29	160	0.93	0.93
20180510	950	1000	10	22.5	5.34	-	170	0.93	-
20180516	950	1000	10	24.2	5.10	3.97	179	0.92	0.90
20180425	950	1000	10	24.2	2.32*	1.98	278	0.88	0.86
20180712	950	1000	50	24.4	5.85	2.55	104	0.96	0.90

* The sample shrunk at the normal stress of 50 kPa prior to the measurement.

** The last thickness before the fracturing or ash generation.

*** Bubble fraction calculated by h_f.

h_i: Initial thickness of the sample

h_f; Final thickness of the sample

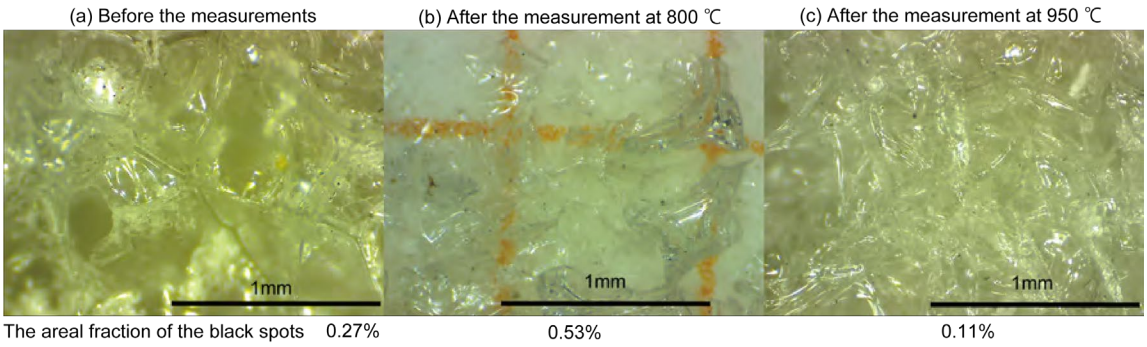

Figure S1: Close up view of the solidified samples observed by a microscope. Transparent films and plateau borders are glass. The black spots are the microlites of the iron titanium oxides. The areal fraction of the black region, including oxides microlites and shades of plateau borders, relative to the glass region, are less than 1 %. Plagioclase microlites could exist but are not recognizable in these photographs. (a) Foamy obsidian baked 1 hour at 1000 ° C, before the rheology measurement. (b) Broken obsidian foam by the rheology measurement at 800 ° C (run number 20180612 in Fig. 2). Red lines are the 1 mm square grid. (c) Deformed obsidian foam by the rheology measurement at 950 ° C (run number 20180425 in Fig. 2).

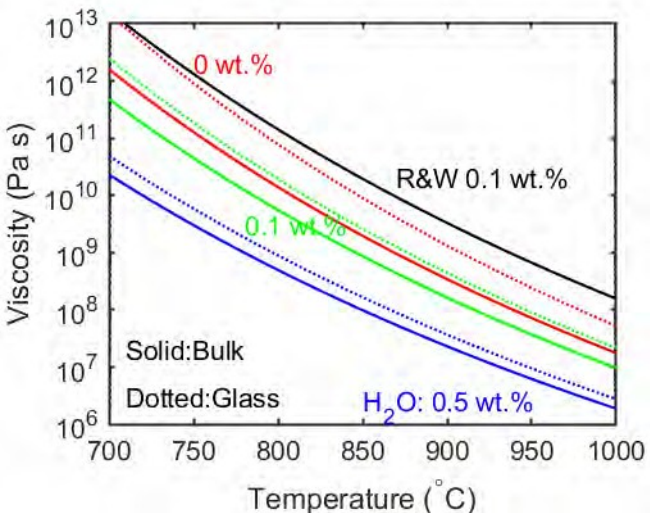

Figure S2: The estimated viscosities of the bubble-free melt of our sample. The red, green, and blue curves are calculated viscosities with the denoted water contents. Solid and dotted curves are for the bulk composition and the glass composition measured by Sano et al. (2015), respectively. These are estimated by Giordano et al., (Giordano et al., 2008). The black curve is estimated by (Romine and Whittington, 2015) for a typical rhyolite composition. We consider that the water content to evaluate the melt viscosity after heating at 1000 ° C, is 0-0.1 wt% (Liu et al., 2005; von Aulock et al., 2017).

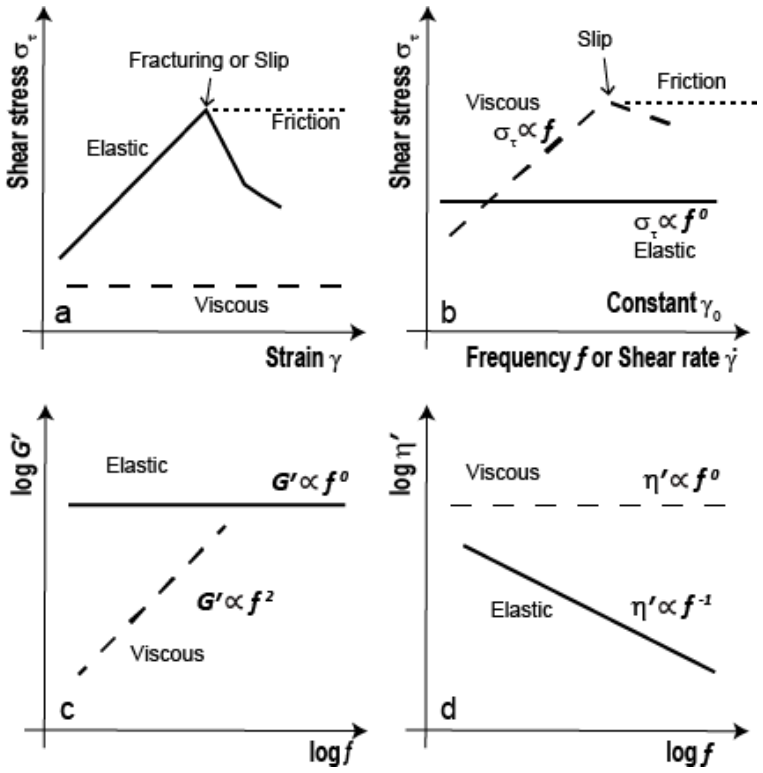

Figure S3: Illustrations of σ_τ, G', and η' curves (e.g., Larson, 1999). The solid, dashed, and dotted curves indicate elastic and viscous materials, and frictional sliding, respectively.

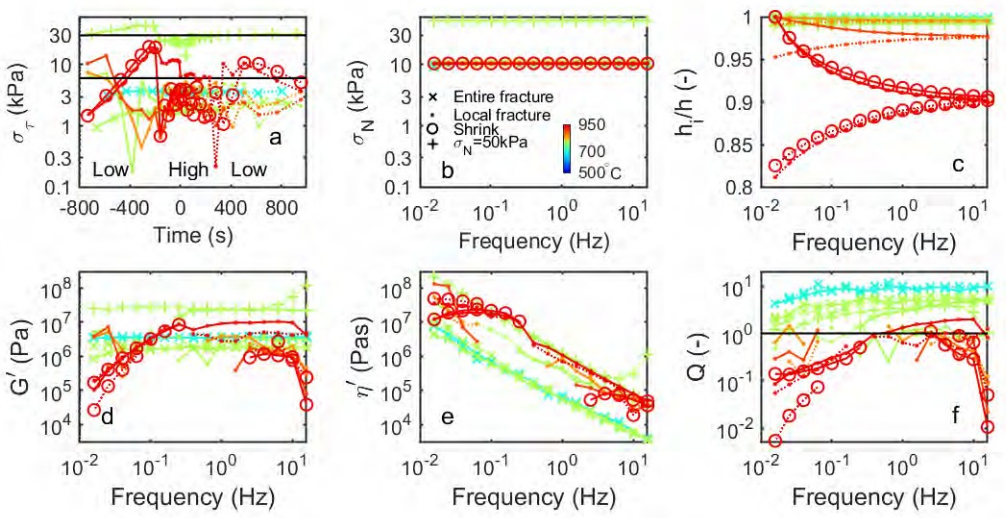

Figure S4: The measured data under oscillatory measurements of the frequency sweep with a constant strain amplitude. (a) Measured shear stress amplitude versus time when data is acquired at each frequency, (b) the normal stress versus frequency, (c) the normalized sample thickness, (d) storage modulus, (e) dynamic viscosity, and (f) inverse of attenuation Q. (d-f) Defined in Eqs.(8-11) in the Methods section. The bluish and reddish colors indicate the lower and higher measuring temperature as denoted in the inset in (b). The symbols indicate the deformation types of samples as denoted in (b) and consist of those used in Fig. 2, in which detailed conditions of measurements are listed. The measurement is conducted by increasing and decreasing the oscillatory frequencies as denoted by the solid and dotted curves, respectively. The frequency change is denoted as "Low, High, Low" in (a). In (a) the black lines show $0.6\sigma_N$, which is 6 or 30 kPa, as a reference of frictional strength. X-axis indicates the relative time to when the frequency is maximum.

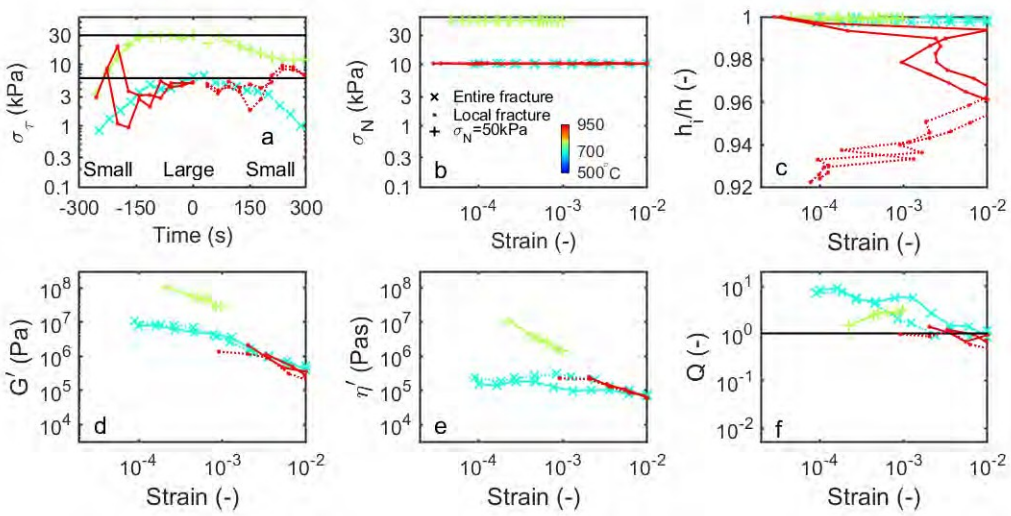

Figure S5: Same as Fig. S4 but for the strain amplitude sweep under a constant frequency of 1 Hz. The solid and dotted curves show the increase and decrease of the strain. In (a), "Small, Large, Small" indicates increase and decrease of the strain. X-axis indicates the relative time to when the strain is maximum.

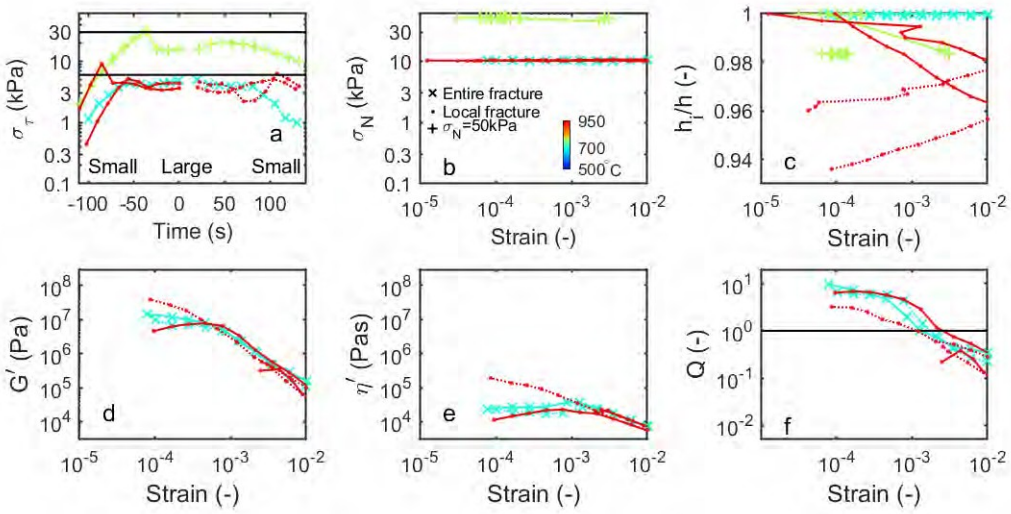

Figure S6: Same as Fig. S5 but for the constant frequency of 10 Hz.

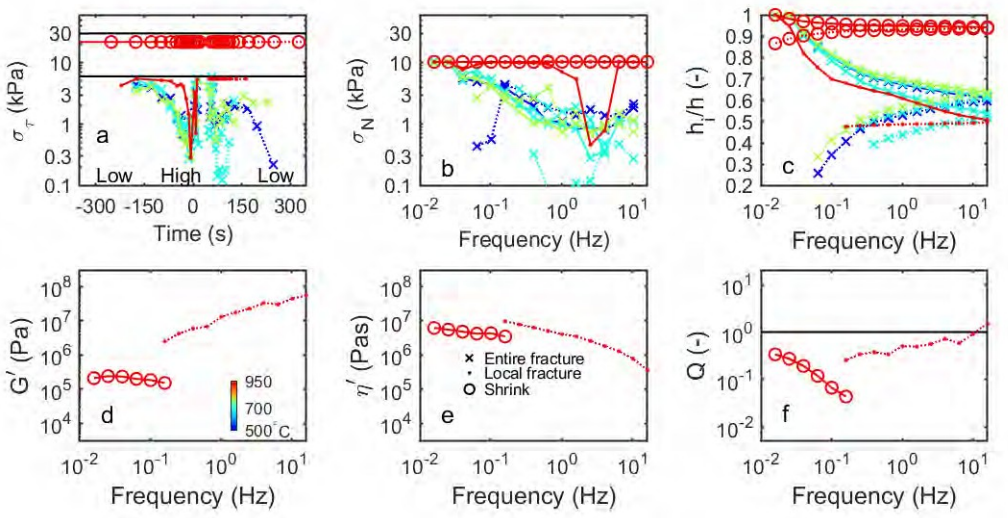

Figure S7: Same as Fig. S4 but for the frequency sweep with a constant stress. The color scale and the legend are shown in the panel (d) and (e), respectively. The measurement is conducted by increasing and decreasing the oscillatory frequencies as denoted by the solid and dotted curves, respectively. In (a), the frequency change is denoted as "Low, High, Low", and x-axis indicates the relative time to when the frequency is maximum.

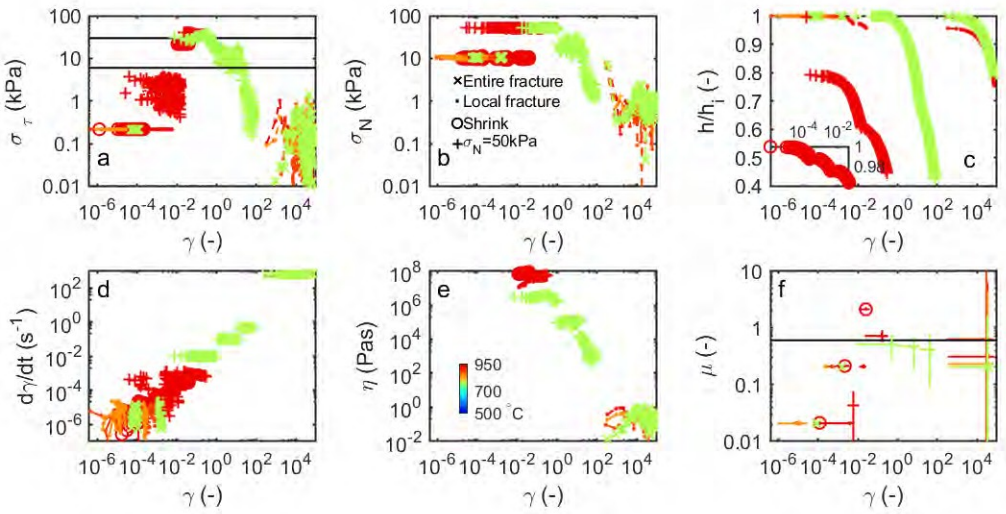

Figure S8: The measured data of one-directional shear deformation. Three preset shear rates or shear stresses are denoted in Fig. 2, and each step is denoted by the solid, dotted, and dashed curves. The symbols and colors are denoted in (b) and (e), respectively, and the same for Fig. S4 and summarized in Fig. 2. (a) The measured shear stress versus total strain, (b) the normal stress, (c) the normalized sample thickness, (d) the shear rate, (e) the apparent viscosity defined by Eq.(6), and (f) the calculated range of the friction coefficient defined by Eq.(7). In (c), the inset shows the measurement of 20180425. In (f) the black line μ = 0.6 is a reference of the friction coefficient.